



# Mechanistic exploration in controlling the product selectivity via metals in TiO<sub>2</sub> for photocatalytic carbon dioxide reduction

Shreya Singh<sup>a</sup>, Raushan Kumar<sup>b</sup>, Kamal K. Pant<sup>a,\*</sup>, Sushant Kumar<sup>b</sup>, Dhavalkumar Joshi<sup>a,c</sup>, Pratim Biswas<sup>d</sup>

<sup>a</sup> Indian Institute of Technology Delhi, Hauz Khas, India

<sup>b</sup> Indian Institute of Technology Patna, Bihta, Patna, Bihar, India

<sup>c</sup> School of Mechanical and Aerospace Engineering, Gyeongsang National University, South Korea

<sup>d</sup> Washington University in St. Louis, St. Louis, MO 63130, USA

## ARTICLE INFO

### Keywords:

Photocatalytic CO<sub>2</sub> reduction  
Reaction mechanism  
DRIFTS  
Product selectivity  
Intermediates

## ABSTRACT

Harnessing the power of the sun, the photocatalytic CO<sub>2</sub> reduction process emerges as a pivotal sustainable solution, utilizing solar energy a premier, clean energy source known for its efficiency and economic viability in the current energy paradigm. This study investigates the impact of metals (Cu, Ag, Au) on enhancing the photocatalytic CO<sub>2</sub> reduction capabilities of TiO<sub>2</sub>. In-depth mechanistic analysis conducted using in-situ DRIFTS for identifying the key reaction intermediates, highlights that the catalytic performance, both in terms of activity and product selectivity, is tightly linked to the underlying reaction mechanisms route, optoelectronic properties, and substrate's (CO<sub>2</sub> and H<sub>2</sub>O) affinities to the catalyst surface. Enhanced light absorption and reduced charge recombination (lifetime enhancement from 0.21 ns to ~1.2 ns) in case of metal incorporated resulted in enhanced overall photocatalytic performance. With Au as dopant, demonstrated highest electron selectivity for H<sub>2</sub> (>97%) compared to Ag and Cu, which showed relatively higher CO<sub>2</sub> reduction electron selectivity (~20% for Cu). The study reveals the crucial interplay of intermediate stabilization, demonstrating its critical role in governing the reaction pathways i.e., carbene or formaldehyde routes as observed in case of Ag and Cu respectively and thus the specific final products. For enhancing the selectivity of CO, engineering the catalyst surface to favour weak CO adsorption is vital. Observations in the CO-TPD measurements demonstrated that Ag sites were effective in promoting the weaker CO\* stabilization thus displayed more selectivity towards CO as compared to Cu. While higher CH<sub>3</sub>OH formation rates in case of Cu, were found to be related to the augmented reactive M=O species stabilization which promotes the oxidation of CH<sub>4</sub> to CH<sub>3</sub>OH. Additionally, in case of Cu, the CH<sub>3</sub>O\* intermediates stabilized effectively, which contributed to more Methanol selectivity through favoured formaldehyde route. While in case of Ag, the CH<sub>2</sub>\* stabilization suggests more probability of the carbene pathway in comparison to the formaldehyde route (as in case of Cu) for producing the CH<sub>4</sub> as the final hydro-generated C1 product. These insights guide the strategic design of catalysts for controlling the reaction pathways and thus selective C1 product production in photocatalytic CO<sub>2</sub> reduction, offering insights for advanced catalyst design.

## 1. Introduction

Titanium dioxide (TiO<sub>2</sub>) has long been recognized as a versatile and robust photocatalyst, due to its various environmental and energy-related applications. Its outstanding chemical stability, non-toxic nature, and strong catalytic ability under ultraviolet (UV) light irradiation positions it as one of the most appealing photocatalytic materials for

both laboratory-scale investigation and industrial applications [1–4]. The use of TiO<sub>2</sub> as a photocatalyst in water splitting (H<sub>2</sub>O) and carbon dioxide (CO<sub>2</sub>) reduction shows great potential, meeting the urgent demand for sustainable energy solutions and carbon-neutral approaches. Nevertheless, its effectiveness is somewhat limited due to a relatively wide bandgap (~3.2 eV) and the rapid recombination of charge carriers, which hampers its catalytic performance [5,6]. Numerous modifications

\* Corresponding author.

E-mail addresses: [shrsingh183@gmail.com](mailto:shrsingh183@gmail.com) (S. Singh), [raushan\\_2221cb13@iitp.ac.in](mailto:raushan_2221cb13@iitp.ac.in) (R. Kumar), [kkpant@chemical.iitd.ac.in](mailto:kkpant@chemical.iitd.ac.in) (K.K. Pant), [sushantkumar@iitp.ac.in](mailto:sushantkumar@iitp.ac.in) (S. Kumar), [dhvlnjoshi@gmail.com](mailto:dhvlnjoshi@gmail.com) (D. Joshi), [pbiswas@wustl.edu](mailto:pbiswas@wustl.edu) (P. Biswas).

<https://doi.org/10.1016/j.apcatb.2024.124054>

Received 30 January 2024; Received in revised form 22 March 2024; Accepted 6 April 2024

Available online 8 April 2024

0926-3373/© 2024 Elsevier B.V. All rights reserved.

to TiO<sub>2</sub>, such as doping with non-metals, metal loading, and surface regulation/engineering, have been extensively explored to boost its photocatalytic efficiency [7–12]. These modification approaches aim to extend its light absorption into the visible range, increase the separation efficiency of photo-generated charge carriers, and improve its surface reaction kinetics.

The band edge alignment of TiO<sub>2</sub> is more conducive to hydrogen evolution reactions (HER) rather than CO<sub>2</sub> reduction, primarily due to its lesser negative conduction band potential. This inherent bias towards H<sub>2</sub> production has prompted several efforts to develop methods for modifying the TiO<sub>2</sub> surface to enhance its ability to reduce CO<sub>2</sub>. Cocatalyst inclusion, deposition and doping with hetero elements are emerging as effective strategies to introduce additional active sites, thereby improving the photoreduction of CO<sub>2</sub>. Studies indicate that the presence of Lewis acid sites in the TiO<sub>2</sub> matrix can significantly influence the CO<sub>2</sub> photoreduction performance [13,14]. Notably, the precise control of these acid sites can regulate the rates and selectivity of CO and CH<sub>4</sub> production. For instance, an engineered photocatalyst with 1 wt% silver doped in mesoporous TiO<sub>2</sub> demonstrated a substantial enhancement in the selectivity and yield of CH<sub>4</sub> [15]. Other transition metals possessing acidic nature like Ce-doped and Cu–Ce-codoped in TiO<sub>2</sub> nanocrystals have demonstrated promising results, particularly in alcohol production rates in an optofluidic microreactor, and showed stability for extended operation times. The enhanced rates can occur due to varying reaction mechanism, as in case of incorporation of Pd nanoparticles on TiO<sub>2</sub>, it illustrated the further amplification in the process by increasing H<sup>+</sup> coverage and promoting protonation of intermediates through hydrogen spillover. This synergistic effect between the ordered oxygen vacancies and hydrogen spillover has led to a notable preference for C<sub>2</sub> products [16]. The valence states of the transition metal also affect the reduction tendency. Research indicates that Cu species, particularly Cu<sup>+</sup> and Cu<sup>0</sup>, can synergistically enhance the photocatalytic efficiency. This enhancement is largely attributed to the creation of defect sites like oxygen vacancies and the Ti<sup>3+</sup> state, which facilitate CO<sub>2</sub> adsorption and electron transfer dynamics, leading to significant increases in CO and CH<sub>4</sub> production under solar radiation [17]. Utilizing the precious metals like Ag, Au has widely been explored [18–20]. Silver-enriched TiO<sub>2</sub> powders synthesized via the sol-gel process have showcased that the interplay of silver impurity bands and the formation of metallic clusters within the TiO<sub>2</sub> matrix can dramatically increase the photocatalytic yield of methane and methanol [19]. The role of silver was twofold: enhancing electron-hole pair generation and prolonging their lifetime through effective spatial separation. The incorporation of bimetallic Au/Ag nanoparticles on TiO<sub>2</sub> nanowires has further demonstrated an impressive absorption of visible light, attributable to localized surface plasmon resonance (LSPR). This phenomenon underpins a significant increase in photoactivity, particularly in the reduction of CO<sub>2</sub> to CO, underscoring the synergistic effects of plasmonic metal nanoparticle decoration [19]. Expanding the scope, the utilization of silver particles to exploit the SPR effect has been proven very effective. By anchoring Ag on cubic phase Li<sub>x</sub>TiO<sub>2</sub>, an increase in CO<sub>2</sub> adsorption and selective CH<sub>4</sub> conversion was observed, with the introduction of Li<sup>+</sup> ions serving to generate beneficial oxygen vacancies [20]. Remarkably, this strategy enhances CH<sub>4</sub> yields significantly under both UV and visible light, with selectivity shifting notably towards CH<sub>4</sub> generation in the presence of Ag. The strategic deposition of Au nanoparticles on TiO<sub>2</sub> has revealed a profound influence on product distribution in CO<sub>2</sub> photoreduction. Low gold loadings have yielded methanol, formic acid, and formaldehyde in the liquid phase, alongside gaseous CO, CH<sub>4</sub>, and H<sub>2</sub> [18].

Other metals have also been used in various studies, which demonstrated that metals like Pt, Pd, Ce, Ag, Au, and Cu, can significantly enhance the photocatalytic efficiency of TiO<sub>2</sub> [15,16,18–22]. These enhancements are achieved either through co-catalyst incorporation or surface deposition. Different metals modify TiO<sub>2</sub>'s electronic properties and create additional sites for enabling the CO<sub>2</sub> reduction. Analysis of different transition metal-modified photocatalysts, using diverse

characterization methods, highlights the importance of catalyst design in fine-tuning product distribution. Each metal contributes uniquely to TiO<sub>2</sub>'s catalytic behaviour, for instance the Ag aids in charge separation and introduces plasmonic effects; Au features a low electron affinity which helps in trapping charge carriers, while Cu showed the additional mid-gap states beneficial for multi-electron transfer processes [18,23]. The selected metals can not only influence the photocatalyst's activity but also can regulate the product selectivity. For example, TiO<sub>2</sub> doped with Ag typically produces more oxygenates, while Cu doping favours hydrocarbon formation [17,19,22]. Understanding the impact of these transition metals on the photocatalytic process and resulting product spectrum is vital for designing catalysts that are optimized for specific reactions.

In this work, we investigate the fundamental reaction mechanisms involved in the photocatalytic CO<sub>2</sub> reduction over TiO<sub>2</sub> modified with different transition metals. Through a systematic study of several phenomena involved in the photoreduction process, the influence on product selectivity of Ag, Au, and Cu based TiO<sub>2</sub> photocatalyst is analysed. Through this investigation, we seek to establish a clear linkage between metal type, reaction intermediates, and product distribution and understand the delicate interplay between metal type, substrate adsorption, and activation barriers for various intermediates as a key to tailoring the product selectivity. The observations can be expected to be crucial in designing catalyst materials that not only enhance CO<sub>2</sub> reduction performance but also provide precise control over the product selectivity, thus contributing to the advancement in the selective photocatalytic CO<sub>2</sub> transformations for sustainable chemical synthesis.

## 2. Materials and methods

### 2.1. Synthesis of pristine TiO<sub>2</sub> nanoparticles

In a 25 ml beaker, 10 ml of Acetic acid (Sigma-Aldrich) was introduced, followed by the addition of 5 ml of Titanium tetra iso-propoxide. The resulting solution was stirred using a magnetic bar until it achieved a transparent yellow color (Step-1). Subsequently, 25 ml of water was added dropwise from a burette at a rate of 2.5 ml/min under vigorous stirring. Initially, the addition of water led to the formation of a white precipitate, which persisted until 3 ml of water was added. At this point, the precipitate was disrupted using a glass rod through continuous stirring. The solution then returned to a transparent state, and the addition of water was continued (Step-2). The stirring process was sustained for an additional 15 minutes before transferring the solution to a preheated hot-air oven set at 50 °C. The solution was left undisturbed in the oven for 12 hours, resulting in the formation of a bluish gel representing the TiO<sub>2</sub> network (Step-3). Subsequently, the as-prepared gel was subjected to heating at 120 °C for 1 hour to eliminate the acetic acid content, yielding TiO<sub>2</sub> powder. To obtain crystalline anatase TiO<sub>2</sub> nanoparticles, the as-prepared powder was further heated at 500 °C for 30 minutes, with a heating rate of 50 °C/min.

### 2.2. Synthesis of Ag/Au/Cu incorporated TiO<sub>2</sub> nanoparticles with controlled concentrations

To prepare Ag/Au/Cu incorporated TiO<sub>2</sub> nanoparticles, the same process as mentioned earlier was employed with a modification in Step-2. Instead of using pure water, a solution containing AgNO<sub>3</sub>, AuCl<sub>3</sub>, and Cu(NO<sub>3</sub>)<sub>2</sub>·3H<sub>2</sub>O in appropriate proportions was mixed with water and added to the TiO<sub>2</sub>-Acetic Acid mixture obtained in Step-1. The amounts of the precursor solution were varied according to Table S2 to achieve 0.1, 0.25, 0.5 and 1 wt% of metal incorporated TiO<sub>2</sub> nanoparticles. The naming of the doped catalyst material from now on is systematically expressed by the molar ratio (X=0.1, 0.25, 0.5, 0.75 and 1)-M (metal Ag, Au or Cu) with host-material (TiO<sub>2</sub>), even if TiO<sub>2</sub> is not included in representation, expressed as X-M or X-M-TiO<sub>2</sub> or M-TiO<sub>2</sub>. All the metal-based TiO<sub>2</sub> samples were subjected to heating at 120 °C for 1 hour to

eliminate acetic acid and subsequently annealed at 500°C to obtain crystalline M-TiO<sub>2</sub> nanoparticles. Fig. S1 represents the respective variations in the subsequent synthesis step of TiO<sub>2</sub> and M-TiO<sub>2</sub> nanoparticles.

### 2.3. Characterization methods

Rigaku benchtop instrument Miniflex-600 X-Ray diffractometer model with CuK<sub>α</sub> ( $\lambda = 1.54 \text{ \AA}$ ) was used to analyse the crystal phase of the catalyst materials. For morphology analysis the field emission scanning electron microscopy images were obtained on FESEM Japan JEOL model JSM-7800 F Prime instrument with photocatalyst samples mounted on carbon coated paper followed by gold coating. The microstructure identification was probed by high resolution transmission electron microscopy (HR-TEM) images obtained on TEM, FEI Tecnai G2 with 200KV accelerating voltage and 10 nm resolution of the catalyst samples suspended uniformly in ethanol solution on copper grid. STEM images and elemental mapping was done using same grid samples obtained using TESCAN unit. The thermal behaviour of the catalyst materials was analysed using TA-instrument with heating from 25°C to 900°C under air environment. The elemental composition, and chemical state was identified using X-ray photoelectron spectroscopy (XPS) measurement performed in Thermo Scientific Nexsa G2 instrument with provision of UPS (Ultraviolet Photoelectron Spectroscopy) measurement. Specific surface area and pore size of the catalyst samples were analysed using Brunauer–Emmett–Teller (BET) analysis from nitrogen adsorption-desorption isotherm with nitrogen adsorption at  $-196.15^\circ\text{C}$  and degassing at 200°C for 6 hrs. The carbon dioxide adsorption capacity of the synthesized catalysts was measured using CO<sub>2</sub> Temperature programmed desorption (TPD) using Quantachrome Chemisorb apparatus by degassing the catalyst sample at 200°C for removal of moisture and other volatile components (methodology in SI section). Same setup was utilized to study the reduction characteristics of the catalyst materials using H<sub>2</sub>-TPR measurements. Cary UV-4000 instrument was used to obtain the UV–vis diffuse reflection spectra (DRS) of the as-prepared photocatalysts using BaSO<sub>4</sub> as internal reflectance standard over wavelength range of 200–800 nm. Photoluminescence spectra (PL) were obtained on fluorescence spectrophotometer Fluoromax-4, Horiba Jobin Yvon Japan model with 280 nm as the excitation wavelength for determination of recombination tendency and the fluorescence lifetime of electron hole pairs. The electrochemical impedance spectroscopic (EIS) & linear sweep voltammetry studies were conducted on Metrohm Autolab 302/PGSTAT electrochemical instrument on lab built three electrode configurations with counter electrode (platinum wire), reference electrode (saturated Ag/AgCl) and working electrode (synthesized photocatalysts) to evaluate the charge transfer property of the as synthesized photocatalyst samples. Photocurrent measurements were performed in 0.1 M Na<sub>2</sub>SO<sub>4</sub> as electrolyte.

### 2.4. In-situ DRIFTS analysis for reaction mechanism

In-situ diffuse reflectance infrared spectroscopic (DRIFTS) analysis was executed in Thermo Scientific Nicolet is50 infrared spectrometer, equipped with the praying mantis chamber from HARRICK with high temperature reaction cell. The cell was equipped with two KBr windows and one quartz window. Firstly, 5 mg of the photocatalyst sample (KBr: photocatalyst weight ratio of 100:1) was loaded into the DRIFTS cell and kept at 110°C under N<sub>2</sub> flow for 30 minutes, this is to purge out any surface impurities. Subsequently, the background spectrum was collected. After this, a combination of CO<sub>2</sub> and water vapor was fed into the system (flow rate of CO<sub>2</sub> was 30 ml/min at room temperature); this was achieved by flowing CO<sub>2</sub> through a bubbler with DI-water. The flow of moist CO<sub>2</sub> gas continued for 60 minutes to saturate the catalyst surface with adsorbed reactive substrates. During the adsorption duration, the absorbance data were recorded at regular intervals over wavenumber 700–4000 cm<sup>-1</sup>, with the spectral resolution of 4 cm<sup>-1</sup> over 64

scans. To catalyse the reaction, light (300 W Xenon lamp) was irradiated through the quartz window for a duration of 100 minutes. Notably, prior to the illumination, baseline data was collected at the zero-minute mark. Post-illumination, spectral data was recorded at regular intervals till 100-minutes. The absorbance data were recorded for 100 minutes over wavenumber 700–4000 cm<sup>-1</sup>, with the spectral resolution of 4 cm<sup>-1</sup> over 64 scans.

### 2.5. Photocatalytic reaction experiments

Photocatalytic CO<sub>2</sub> reduction experiments were conducted using top illuminated stainless steel reactor system similar to that employed in our previous study [24]. Water was used as the source of hydrogen and Triethanolamine (10%) was utilized as a hole scavenger. A 250 W medium pressure mercury vapor lamp was used as the light source. A fixed amount of powder photocatalyst (5.0 mg) was evenly dispersed in 5 ml DI water and TEOA, ultrasonicated for 5 min to make a uniform solution, the mixture was then introduced into the reactor and uniform stirring was maintained at 1000 rpm to keep the catalyst in the suspension and overcome the mass transfer limitations. The system is then purged several times with N<sub>2</sub> to remove any impurities present in the solution and then the high purity CO<sub>2</sub> (99.99%) was introduced, regulated by a mass flow controller at a flow rate of 3 ml/min passed through the solution for 45 min to make the system saturated with CO<sub>2</sub> until During an entire photoreduction experiment, the system was illuminated and left undisturbed to form the CO<sub>2</sub> reduced product. The liquid products were measured by a gas chromatograph (GC, Agilent 7820 A) equipped with DB-WAXETR column in a flame ionization detector (FID), while the gas samples were measured in gas chromatograph CS-5800 model from Centurion Scientific. This instrument was equipped with a methanizer and dual detectors: a Flame Ionization Detector (FID) and a Thermal Conductivity Detector (TCD). For separation, the system employed HYSEP-A and Molecular Sieve 5 Å columns, which were connected via a switching arrangement.

## 3. Results and discussion

### 3.1. Crystal phase and structures

The TiO<sub>2</sub> sample was prepared by sol-gel method, as illustrated in materials and method section. The X-ray diffraction (XRD) analysis of the as-prepared TiO<sub>2</sub> sample indicated that the major contribution was from the anatase phase in the formed TiO<sub>2</sub> material (Figure S1).

The doping of metals in TiO<sub>2</sub> was done through the addition of the metal-salt solution (details in Table S2) in the step before the gel formation with subsequent steps remaining same. It was observed that in all the M-TiO<sub>2</sub> samples, the anatase phase was predominantly present (Fig. 1A,B,C), without a significant detection of metal oxide phases or free metallic phase, suggesting a high dispersion of the metal dopants in the TiO<sub>2</sub> lattice. For various M-TiO<sub>2</sub> with M= Ag, Cu, and Au the metal loading amount was varied from 0.1 wt% to 1 wt%. Beyond this point, typically above 1 wt% loading, the XRD patterns suggested the onset of solid solution formation where the dopants may exceed the solubility limit in the TiO<sub>2</sub> lattice, leading to the formation of a separate phase or aggregation of metal clusters instead of being doped. The degree of doping, as well as the specific metal characteristics in terms of ionic radii, oxidation states, M-O/M-Ti interactions, play a critical role in determining the dissolution potential of dopant in the lattice of TiO<sub>2</sub>. The XRD patterns as presented in Fig. 1 A, B, C, reveals the comparative diffraction patterns with the incorporation of various metal dopants (Ag, Cu, Au) at different loadings. Notably, the absence of distinct diffraction peaks corresponding to the individual metals suggest that Ag, Cu, and Au does not form separate phases (metal or metal-oxide) but are instead well incorporated [25,26]. Although, no distinct phase formation occurs but there are slight alterations in the diffraction patterns of anatase TiO<sub>2</sub> phase. A slight peak shift corresponding to the 101 plane of TiO<sub>2</sub> after



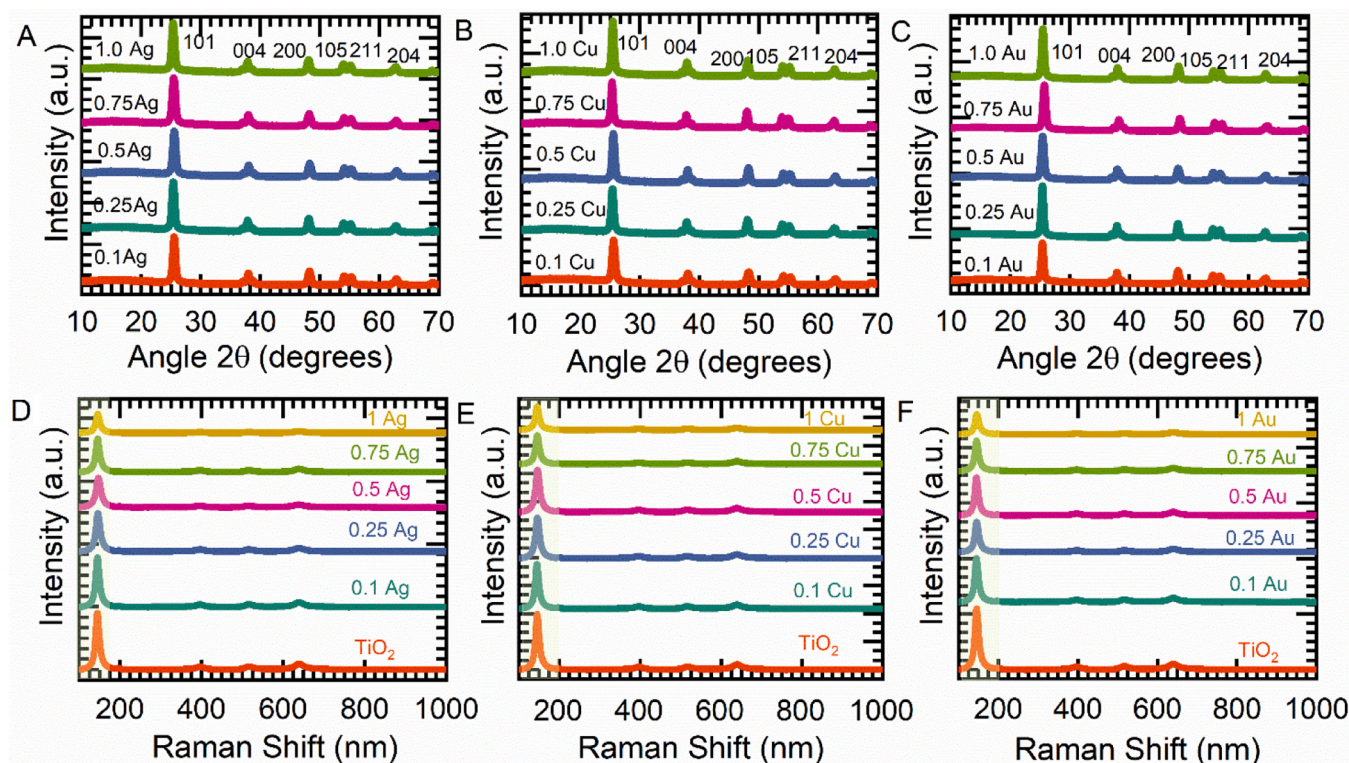


**Fig. 1.** (A, B, C) XRD patterns for different M-TiO<sub>2</sub> (M=Ag, Cu, Au) nanocrystals marked with miller indices of different diffraction planes in TiO<sub>2</sub> with varied metal loading amounts (D, E, F) Raman spectra of TiO<sub>2</sub> doped with Ag, Cu, Au, (from left to right) at concentrations from 0.1 to 1 wt% of metal dopant.

the incorporation of different metals is observable (Figure S3). The peak shift direction in the case of Cu and Ag based TiO<sub>2</sub> differs from that observed in case of Au (Fig. 1 A,B,C and S3). Low angle shift, or a left shift, was observable for Cu and Ag, which increased with increasing metal loading amount (Figure S3), while right shift toward higher angles was noticeable for Au. These different diffraction trends suggests different dopant interactions in case of Au when compared to those in case of Ag and Cu. Fundamentally, the oxidation state of the metal species present in the structure, their atomic radii and the strength of M-O/M-Ti interactions are among the crucial factors determining the shifts in diffraction patterns [25,26]. From the X-ray photoelectron spectroscopy (XPS) findings presented in Fig. 4 (discussed in detail later), it is observed that Au is incorporated into the TiO<sub>2</sub> lattice in the form of Au<sup>3+</sup>, whereas Ag and Cu are present as Ag<sup>+</sup> and Cu<sup>+</sup>, respectively. This distinction is significant as the smaller ionic radius of Au<sup>3+</sup> (82 pm) compared to Ag<sup>+</sup> (115 pm) and Cu<sup>+</sup> (96 pm) ions is the actual factor causing the observed shift of XRD peaks towards higher degrees for samples doped with Au. This phenomenon can be attributed to the more considerable lattice contraction resulting from the substitution of TiO<sub>2</sub> sites with the smaller Au<sup>3+</sup> ions, leading to a reduction in the lattice parameter and consequently, a shift in the diffraction peaks towards higher angles. Furthermore, metal-Ti repulsion and metal-O attraction as critical factors influencing the changes in lattice size, beyond the simplistic view of ionic radii effects. Hence, it can be interpreted that in the case of Cu and Ag doping, the observed left shift (towards lower angles) is attributed to tensile strain, indicating an expansion of the TiO<sub>2</sub> lattice. Conversely, for Au doping, the right shift (towards higher angles) is an indicative of the compressive strain caused in TiO<sub>2</sub> lattice [26,27].

The Raman spectroscopic analysis of TiO<sub>2</sub> doped with Ag, Cu, and Au metals provides a crucial insight into the structural modifications, the similar spectral trend (Fig. 1D,E,F) suggests the preservation of the anatase phase integrity post-doping in all the metal based TiO<sub>2</sub> catalysts. The characteristic vibrational modes at 144, 197, 399, 515/519, and 639 cm<sup>-1</sup> which corresponds to E<sub>g</sub>, E<sub>g</sub>, B<sub>1g</sub>, A<sub>1g</sub>/B<sub>1g</sub>, and E<sub>g</sub> symmetries

of the anatase phase, respectively, are retained [28]. The absence of origin of any new Raman bands or substantial shifts in the spectra is an indicative that the metal dopants are uniformly integrated into the TiO<sub>2</sub> lattice. This uniformity precludes the formation of separate metallic or oxide phases within the detection limits of the spectral analysis, however from XRD it was already observed to not be forming any distinct phase. In the doped TiO<sub>2</sub> samples, slight frequency shifts in the main E<sub>g</sub> Raman band around 144 cm<sup>-1</sup> indicate the presence of metal-induced oxygen vacancy [28]. These vacancies, can arise from multiple reasons, and charge imbalances due to the substitution of metal ions with various oxidation states for Ti<sup>4+</sup> ions, can be one which could lead to lattice distortions, which is observable by the peak broadening corroborating well with those observed in case of diffraction patterns and confirming the substitutional doping dominance for Au in TiO<sub>2</sub> matrix compared to Cu and Ag [28]. The presence of oxygen vacancies is observed by a reduction in Raman peak intensity and an enlargement of the full width at half maximum (FWHM), particularly in the narrow spectral range (Figure S4). Specifically, Au doping in TiO<sub>2</sub> is associated with a more pronounced creation of oxygen vacancies, possibly due to the incorporation of higher atomic radii of Au on the TiO<sub>2</sub> surface [28]. The formation of these oxygen vacancies consequently results in the electronic interactions with the TiO<sub>2</sub> lattice, which subsequently can introduce a strain in the TiO<sub>2</sub> lattice. This strain, in turn, manifests as localized distortions within the crystal matrix as observed from lattice parameters variations as found in the XRD analysis. The observed variations in peak intensity and FWHM across the Raman spectra signify the extent of metal incorporation and the resultant strain or defects in terms of formation of oxygen deficient sites within the TiO<sub>2</sub> lattice which could contribute as an important factor for optimizing TiO<sub>2</sub>'s photocatalytic attributes.

### 3.2. Surface area and thermal stability

The thermal stability of different M-TiO<sub>2</sub> materials were studied



through thermogravimetric analysis (TGA). From the TGA profiles (Fig. 2A), it is observed that the weight loss profiles for Cu/TiO<sub>2</sub>, Ag/TiO<sub>2</sub>, and Au/TiO<sub>2</sub> differs, reflecting the differed impacts of different metals on the thermal behaviour of TiO<sub>2</sub>. Notably, the Cu/TiO<sub>2</sub> sample begins to lose weight at a lower temperature compared to Ag/TiO<sub>2</sub> and Au/TiO<sub>2</sub>, suggesting that the Cu incorporation could be influencing the thermal stability of the material, possibly due to the formation of less stable interactions with the TiO<sub>2</sub> lattice which can decompose at lower temperatures [29]. Further, other factors can also be attributed to the difference in nature of TGA profiles, including the nature of the interaction with metals, the stability of the metal species within the TiO<sub>2</sub> matrix, and the thermal properties of the metals themselves. Possibly due to lower atomic size, different oxidation state or the coordination environment in the TiO<sub>2</sub> matrix, lower decomposition temperature for Cu is observed [29]. Here based on the phase structure, copper is expected to undergo oxidation or other chemical changes at lower temperatures compared to gold or silver compounds, which are relatively more thermally stable. Additionally, copper exists in several oxidation states, commonly Cu<sup>0</sup>, Cu<sup>+</sup>, and Cu<sup>2+</sup>, and can also transit between these states upon heat treatment [30]. The TGA profile indicates such transitions, are not as prevalent for the case silver and gold and the thermal profile is similar to that in case of undoped TiO<sub>2</sub>. The nitrogen adsorption-desorption isotherms analysed by Brunauer-Emmett-Teller (BET) method reveals the surface adsorption characteristics of these materials, the profiles in Fig. 2B, depicts the presence of a type IV isotherm with a H2 hysteresis loop, which is characteristic of mesoporous materials [31]. H2 hysteresis loop is typically associated with materials that have pore structures resembling ink-bottle shapes or pores that are wider on the inside than at the entrance.

This type of loop exhibit a plateau at high relative pressures, which is consistent with the presence of mesopores, which is a common feature in materials with the presence of wider pore sizes. Table 1 demonstrates the pore volume, mean pore diameter and specific surface areas for M-TiO<sub>2</sub>. Furthermore, the hysteresis observed in these isotherms is an indicative of mesoporosity, which can be beneficial for the diffusion of reactants and products during the catalytic reaction processes. The increase in adsorption volume at higher relative pressures (P/P<sub>0</sub> approaching 1) for Au/TiO<sub>2</sub> particularly highlights its significant mesoporosity compared to Ag/TiO<sub>2</sub> and Cu/TiO<sub>2</sub>, indicating a higher surface area or more open pore structure in Au/TiO<sub>2</sub>.

### 3.3. Morphology and textural characteristics

The evaluation of the particle sizes and its distribution obtained through analysis using ImageJ software is represented in the curves as shown in Figure S7 for M-TiO<sub>2</sub> samples. The particle size distribution

**Table 1.**

Pore characterization of TiO<sub>2</sub> and metal doped TiO<sub>2</sub> catalysts: total pore volume, micropore volume (V<sub>m</sub>), BET surface area (S<sub>a,BET</sub>), and mean pore diameter.

Catalyst	Total pore volume (cm <sup>3</sup> g <sup>-1</sup> )	V <sub>m</sub> (cm <sup>3</sup> (STP) g <sup>-1</sup> )	S <sub>a,BET</sub> (m <sup>2</sup> g <sup>-1</sup> )	Mean pore diameter (nm)
TiO <sub>2</sub>	0.19	18.71	81.5	9.53
Cu-TiO <sub>2</sub>	0.18	17.68	76.9	9.61
Ag-TiO <sub>2</sub>	0.16	15.53	67.6	9.48
Au-TiO <sub>2</sub>	0.20	21.59	94.1	8.58

patterns reveal a significant insight into the morphology and distribution of the metals in the catalyst particles. For the Cu-doped TiO<sub>2</sub> (Chart A), the particle size distribution is relatively broad, ranging from 5 to over 40 nm, with a peak in the distribution around 10–15 nm. This suggests a heterogeneous nucleation and growth process during synthesis, leading to a wide variety of particle sizes. In contrast, the Au-doped TiO<sub>2</sub> (Figure S7 Chart B) presents a narrower size distribution, predominantly between 10 and 25 nm, indicating a more uniform particle size which can be due to the substitutional doping in Au, promoting the growth mechanism for TiO<sub>2</sub> and in turn can be advantageous for consistency in catalytic activity. The peak of the distribution is around 15–20 nm, suggesting a controlled growth mechanism that favours the formation of particles within this size range. The Ag-doped TiO<sub>2</sub> (Chart C) shows a particle size distribution like that of Au, with a slight shift towards smaller sizes. The distribution spans from approximately 5 to 35 nm, peaking around 10–15 nm. This indicates a relatively uniform synthesis process with a tendency towards the formation of smaller particles compared to Cu and Au. The Transmission Electron Microscopy (TEM) image (Fig. 3A, S5A, S6A) shows the aggregated morphology of the particles, which could affect the catalytic properties by potentially limiting the accessibility of reactants to the active sites.

The High-Resolution Transmission Electron Microscopy (HRTEM) image (Fig. 3B, S4B, S5B), along with the Selected Area Electron Diffraction (SAED) pattern inset, confirm the crystalline nature of the particles, with distinct lattice fringes visible, indicating high degree of crystallinity. The d-spacing (~3.5 Å) corresponding to 101 planes of TiO<sub>2</sub> as evaluated from HRTEM for all the catalyst samples matches well with those observed in the XRD. The SAED pattern (Fig. 3B, S4B, S5B inset), demonstrates the polycrystalline nature of the catalyst, which is typical for the nanoparticles that have grown in various orientations, here typically ascribed to TiO<sub>2</sub>. The prominent rings observed in the diffraction patterns can be indexed to the anatase TiO<sub>2</sub> crystal planes of (101), (004), (105), (200), and (204), in all the catalyst samples which indicates the dominant presence of the anatase phase of TiO<sub>2</sub>[28,32,33]. Scanning Transmission Electron Microscopy (STEM) image with

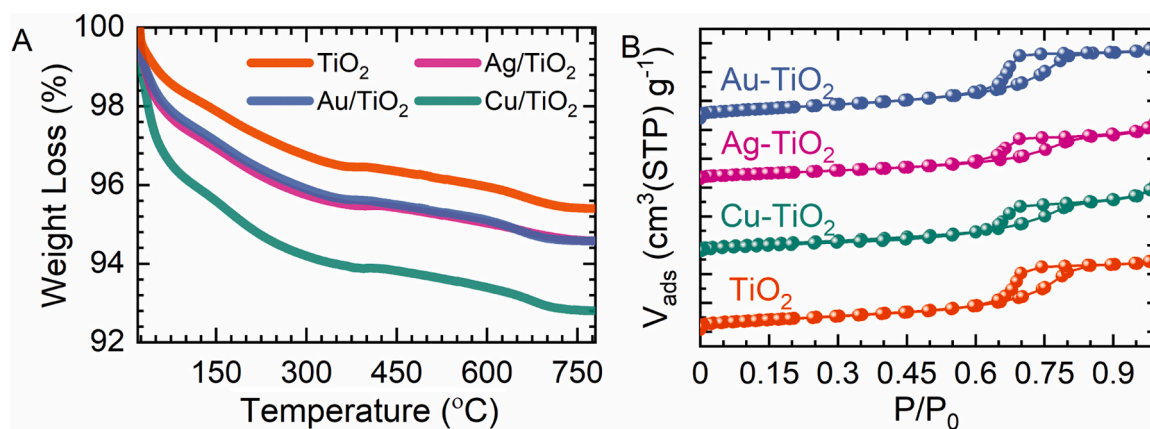


**Fig. 2.** Thermogravimetric analysis (A) and nitrogen adsorption isotherms (B) of TiO<sub>2</sub> doped with Au, Ag, and Cu, showing thermal stability and porosity characteristics, respectively.

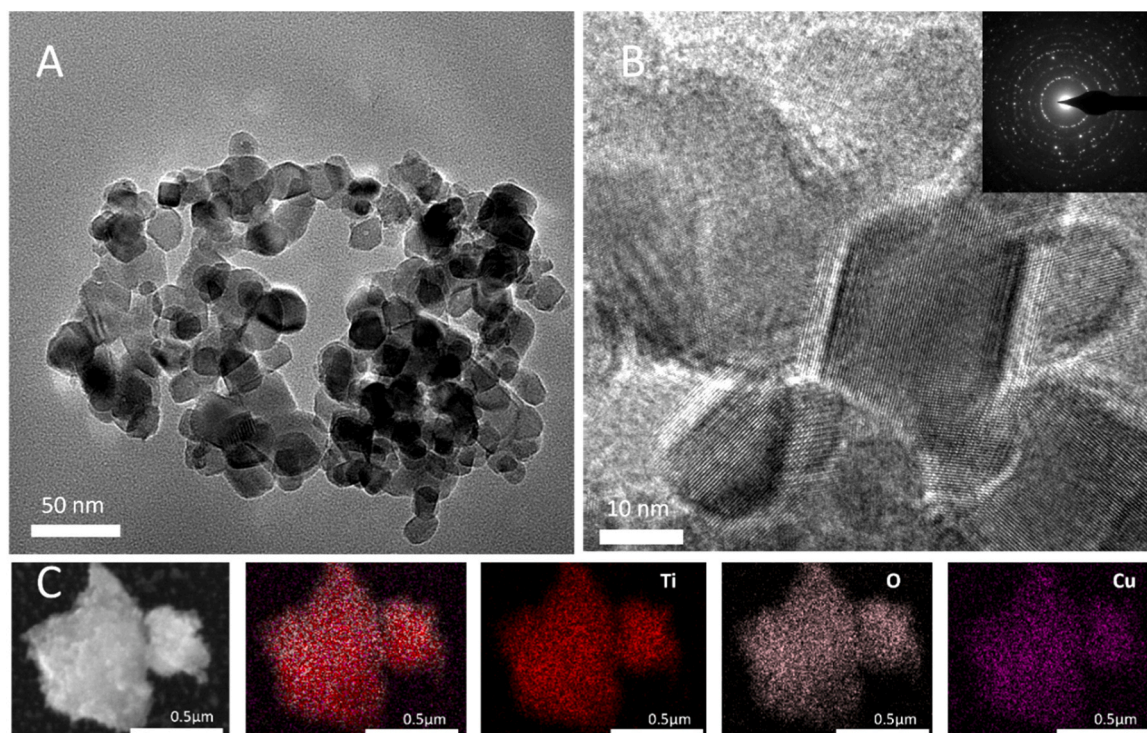


**Fig. 3.** Transmission electron microscopy images of Au/TiO<sub>2</sub> nanoparticles: (A) low magnification, (B) high-resolution with inset showing selected area electron diffraction pattern, and (C) corresponding elemental mapping for O, Ti, and Cu.

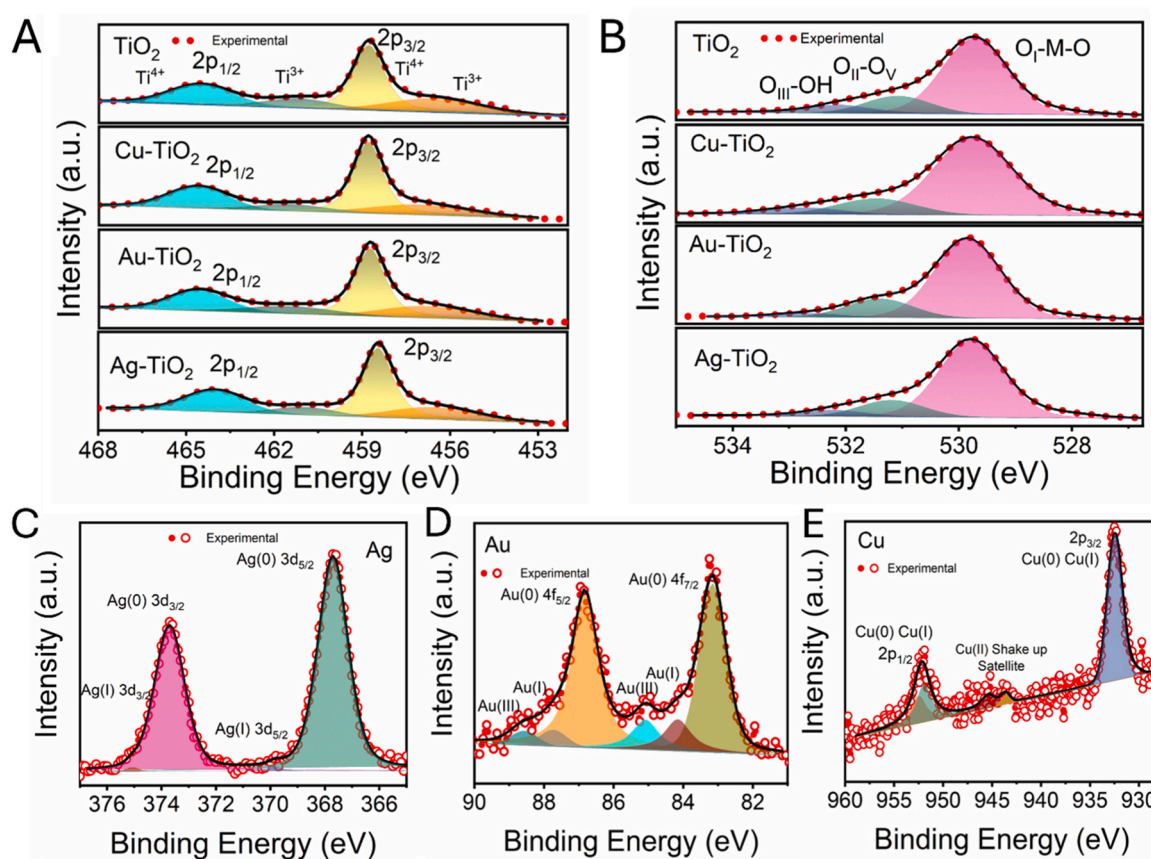


**Fig. 4.** Narrow Scan X-ray photoelectron spectroscopy (XPS) spectra showing the binding energy shifts for (A) Ti 2p, (B) O 1 s, (C) Ag 3d, (D) Au 4 f, and (E) Cu 2p in pure TiO<sub>2</sub> and metal-doped TiO<sub>2</sub> (Cu, Au, Ag) catalyst.



elemental mapping (Fig. 3C, S4C, S5C) of the samples illustrates the spatial distribution of the elements, with Ti and O being uniformly distributed throughout the particles, as expected for TiO<sub>2</sub>. The uniform metal distribution confirms the incorporation of different metals in the M-TiO<sub>2</sub> matrix.

### 3.4. Valence and oxidation state of metals

The X-ray photoelectron spectroscopy (XPS) analysis of M-TiO<sub>2</sub> reveals critical insights into the electronic structure and chemical state of the constituent elements. Ti 2p narrow range XPS spectrum of pure and metal incorporated TiO<sub>2</sub> (Fig. 4A) exhibits two peaks near 458.5 and 464.5 eV, belonging to Ti 2p<sub>3/2</sub> and Ti 2p<sub>1/2</sub> of Ti<sup>4+</sup>, respectively [34]. For M-TiO<sub>2</sub>, the binding energy of Ti 2p<sub>1/2</sub> and Ti 2p<sub>3/2</sub> shifts towards lower binding affinity due to the induced polarization by the metal species and metal ions, indicating the presence metal species in TiO<sub>2</sub>. The red shift was observed to be highest for Ag followed by Au and then Cu. Moreover, in the Ti 2p high-resolution spectra of TiO<sub>2</sub> and M-TiO<sub>2</sub>, the existence of Ti<sup>3+</sup> states is also observed which is indicative of the presence of oxygen vacancies on the surface of TiO<sub>2</sub>. For Cu-TiO<sub>2</sub>, the two peaks at 931.7 and 951.5 eV belong to Cu 2p<sub>3/2</sub> and Cu 2p<sub>1/2</sub>, Cu 2p spectrum (Fig. 4E) reveals the presence of Cu species in the intermediate state of Cu<sup>0</sup> and Cu<sup>+</sup>/Cu<sup>2+</sup> states, suggesting the presence of both substitution of Ti<sup>4+</sup>/Ti<sup>3+</sup> ions by Cu<sup>+</sup>/Cu<sup>2+</sup> ions, and presence of surface adsorbed copper metal species [17]. Similarly, for Ag-TiO<sub>2</sub> and Au-TiO<sub>2</sub>, metal is incorporated both in lattice substitutional form e.g. Ag<sup>+</sup> for Ag-TiO<sub>2</sub> and Au<sup>3+</sup> for Au-TiO<sub>2</sub>, surface adsorbed form (Fig. 4C-D). The high-resolution peaks for Au (Fig. 4D) centered at 83.3 eV and 87.0 eV are assigned to the metallic Au 4f<sub>7/2</sub> and 4f<sub>5/2</sub> spectra, which agrees with typical Au<sup>0</sup> and Au<sup>3+</sup> species [38]. While for the Ag, its 3d spectra (Fig. 4C) confirms the presence of metallic Ag species, with two characteristic peaks near 458.8 and 464.8 eV corresponding to 3d<sub>5/2</sub> and 3d<sub>3/2</sub> respectively [20]. Additionally, the fraction of Ti<sup>3+</sup> was also found to be more in case of Au than in Cu or Ag, possibly due to the substitution preference of Ag and Cu ions near oxygen vacant sites, in contrast to the substitution preference of Au<sup>3+</sup> for Ti<sup>4+</sup> site. The XPS spectra of O 1s of pure TiO<sub>2</sub> (Fig. 4B) show three peaks at 529.95, 531.70 and 532.61 eV, belonging to lattice oxygen (O<sup>2-</sup>), surface adsorbed oxygen species due to surface defects such as oxygen vacancy (O<sub>v</sub>) and surface adsorbed oxygenated species (e.g., OH groups) respectively represented as O<sub>I</sub>, O<sub>II</sub>-O<sub>v</sub> and O<sub>III</sub>-OH [16].

After doping with metal, the proportion of different oxygen present changes and the relative population of different types of oxygens present in M-TiO<sub>2</sub> is tabulated in Table 2. More O<sub>II</sub>-O<sub>v</sub> in Au-TiO<sub>2</sub> indicates adsorbed oxygen-containing groups on the surface indicating a higher density of oxygen vacancies (O<sub>v</sub>) in the Au-TiO<sub>2</sub>. This finding is supported by previous studies where Au-doping was found to be associated with increase in oxygen vacancies near the substitutional site [35].

The H<sub>2</sub>-Temperature Programmed Reduction (H<sub>2</sub>-TPR) profiles for TiO<sub>2</sub> and metal-incorporated TiO<sub>2</sub> (with Cu, Ag, and Au) as shown in Fig. 5, also reveals significant insights into the oxidation states of various metals, reducibility, and metal-support interactions in these catalyst samples. From the TPR profile of pure TiO<sub>2</sub> it displays a distinct reduction peak, which is typically associated with the reduction of surface oxygen species or oxygen vacancies present within the structure of TiO<sub>2</sub> lattice. The peak corresponding to ~450C signifies the inherent

reducibility of the TiO<sub>2</sub> support, but on metal incorporation, the TPR profiles of Cu-TiO<sub>2</sub>, Ag-TiO<sub>2</sub>, and Au-TiO<sub>2</sub> show significantly varied reduction behaviour, indicative of the different interactions between the metal species and the TiO<sub>2</sub>.

The Cu-TiO<sub>2</sub> catalyst (Fig. 5B) exhibits multiple reduction peaks across the temperature range, suggesting the presence of various Cu oxidation states and the corresponding significant shift to lower temperatures (220C) suggests a significant change in the reduction behaviour on the interaction among Cu species and the TiO<sub>2</sub>. The observed phenomenon can be attributed to the 'spillover effect,' where metallic impurities present facilitate the reduction of the oxide. The reduction peaks may correspond to the reduction of CuO to Cu<sub>2</sub>O and further to metallic Cu, indicating the multi-step reducibility of copper oxides [36]. While for the Ag-TiO<sub>2</sub>, the TPR profile (Fig. 5C) shows the shift towards higher temperature (600C) of the prominent reduction peak, which can be attributed to the reduction of Ag<sup>+</sup> species to metallic Ag. While for the Au-TiO<sub>2</sub> the reduction profile (Fig. 5D) presents slight changes in the peak temperature (~500C) reflecting the reducibility of gold species in the TiO<sub>2</sub> matrix. The position of peak gives an indication of the strength of interaction, with a higher temperature peak suggesting stronger interactions and requires more energy (higher temperature) to reduce which can be attributed here to the substitutional doping effect in case of Au [36]. Highest reduction temperature as in case of Ag can possibly be due to the presence of Ag in metallic state as observed in XPS analysis while Cu and Au showing some fraction of other oxidation states thus enabling the reduction at slight lower temperatures. This further affirms the presence of metals in varied oxidation states after being incorporated into TiO<sub>2</sub>.

### 3.5. Optoelectronic properties

In the light assisted reactions, the role of light absorption, charge separation and resistance towards their transport can play significant role in altering the performance. Hence, it is essential to clearly understand the optoelectronic properties of M-TiO<sub>2</sub> catalytic systems to understand the impact on photocatalytic ability. The UV-Vis Diffuse Reflectance Spectra (UV-DRS) of metal-doped TiO<sub>2</sub> (with Ag, Au, and Cu) demonstrates the alterations in the optical properties of TiO<sub>2</sub> due to the incorporation of different metal nanoparticles Fig. 6. For pure TiO<sub>2</sub>, the UV-DRS typically shows high absorption in the UV region due to the electronic transitions from the valence to the conduction band, which is typically attributed to the electronic transition from the valence band (O<sub>2</sub>-2p orbital) to the conduction band (Ti<sup>4+</sup> 3d orbital) [2]. This transition underlines the higher bandgap energy of TiO<sub>2</sub> and is responsible for its photocatalytic activity under UV light. Upon doping with metals (Ag, Au and Cu), the absorption spectra of TiO<sub>2</sub> exhibits a red shift, which can be seen as a broadening of the absorption edge into the visible light range with varied extent depending on the properties of metal dopants. This enhancement stems from the intrinsic O<sub>2</sub>-(2p) → Ti<sup>4+</sup> (3d) transition coupled with the O<sub>2</sub>-(2p) → Cu<sup>2+</sup>(3d) charge transfer processes [30,37]. The presence of Cu introduces additional electronic states within the bandgap, which are observed as absorption bands extending from 600 to 1000 nm. These bands are characteristic of the 2e<sub>g</sub>-2t<sub>g</sub> transitions of Cu<sup>2+</sup> ions in a distorted octahedral symmetry, indicating the integration of Cu into the TiO<sub>2</sub> lattice and potentially the formation of CuO or Cu<sub>2</sub>O species [17,22]. The extended absorption edge suggests narrowing of the bandgap and the presence of Cu species introduces new energy levels within the bandgap or modifies the conduction and valence band edges, facilitating visible light absorption.

The intensity of absorption and the position of the absorption edge in the spectra are influenced by the concentration of the metal dopants [38]. Higher concentrations typically lead to more pronounced absorption in the visible range, indicating a stronger modification of the TiO<sub>2</sub> electronic structure. For the gold (Au) and silver (Ag)-doped TiO<sub>2</sub> samples, the UV-DRS spectra exhibit an additional absorption band in the visible region around 570–650 nm (Fig. 6) [39]. This band is

**Table 2.**  
Relative population of different types of oxygens present in M-TiO<sub>2</sub> as obtained from XPS O1s spectra.

M-TiO <sub>2</sub>	O <sub>I</sub>	O <sub>II</sub>	O <sub>III</sub>
TiO <sub>2</sub>	74.2	15.8	10.0
Cu-TiO <sub>2</sub>	77.6	15.6	6.8
Ag-TiO <sub>2</sub>	82.3	15.0	2.6
Au-TiO <sub>2</sub>	79.0	17.4	3.6



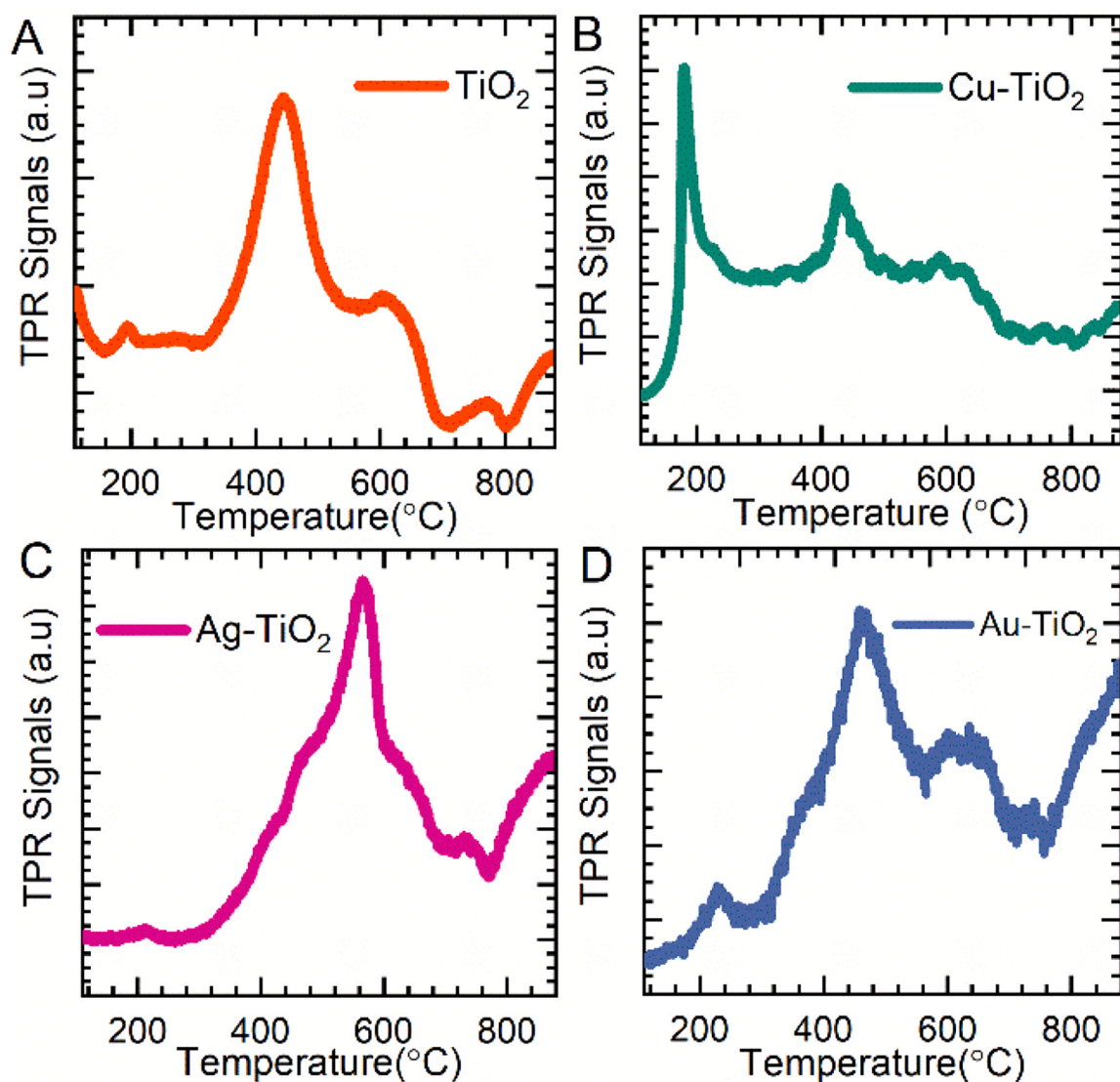


Fig. 5. Temperature-programmed reduction (TPR) profiles of pure  $\text{TiO}_2$  and metal-doped  $\text{TiO}_2$  catalysts: (A)  $\text{TiO}_2$ , (B)  $\text{Cu-TiO}_2$ , (C)  $\text{Ag-TiO}_2$ , and (D)  $\text{Au-TiO}_2$ .

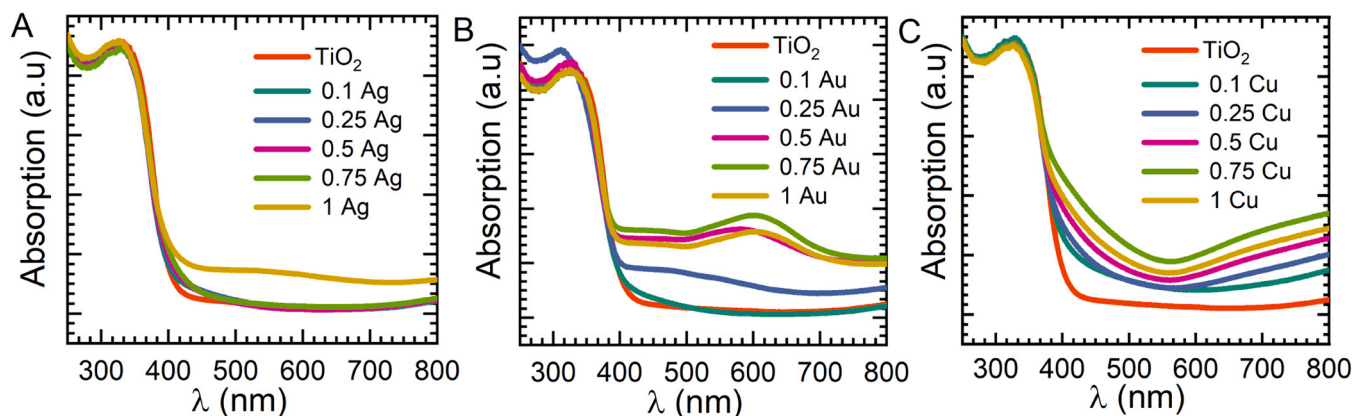


Fig. 6. UV-Vis absorption spectra of  $\text{TiO}_2$  and metal-doped  $\text{TiO}_2$  catalysts with varying metal loadings:  $\text{Ag-TiO}_2$  (left),  $\text{Au-TiO}_2$  (centre),  $\text{Cu-TiO}_2$  (right).

associated with the localized surface plasmon resonance (LSPR) of metallic Ag/Au species. LSPR effect arises from the collective oscillations of free electrons in the Ag/Au nanoparticles under the influence of the electromagnetic field of light. This interaction significantly increases

the absorption of visible light, which is advantageous for photocatalytic applications that utilize solar irradiation. In the case of higher loading in Au-doped  $\text{TiO}_2$ , the spectra show a pronounced absorption in this domain. The presence of metallic Ag/Au/Cu not only introduces new

electronic states that act as charge transfer facilitators but also is expected to prolong the lifetime of photo-generated charge carriers by trapping them at the interface of the  $\text{TiO}_2$ . This synergistic effect can contribute to enhance the photocatalytic efficiency of the M- $\text{TiO}_2$  system under both UV and visible light irradiation [5].

The Photoluminescence (PL) and Time-Resolved Photoluminescence (TRPL) spectra provide valuable insights into the recombination dynamics of photogenerated electron-hole pairs within semiconductor materials. From the obtained PL spectrum (Fig. 7A), it is observed that the emission intensities of  $\text{TiO}_2$  and M- $\text{TiO}_2$  ( $\text{Ag-TiO}_2$ ,  $\text{Au-TiO}_2$ , and  $\text{Cu-TiO}_2$ ) differs. As the PL intensity is an indicator of the recombination rate of charge carriers: lower PL intensity suggests fewer recombination, which is desirable for photocatalytic applications because of the longer-lived charge carriers [24,40,41]. The undoped  $\text{TiO}_2$  sample shows a significant PL intensity, indicating higher rate of electron-hole recombination. Upon doping with metals, the PL intensity decreases in the order of  $\text{Ag-TiO}_2$ ,  $\text{Au-TiO}_2$ , and  $\text{Cu-TiO}_2$  exhibiting the lowest intensity. This suggests that the copper doping most effectively suppresses charge carrier recombination, in addition to the enhanced light absorption, possibly due to the new energy levels that assisted in improved charge separation efficiency.

Further, to quantify the lifetimes of the charge carriers and impact on metal dopants time resolved measurements were carried. The TRPL spectra (Fig. 7B) further provided the charge carrier dynamics by measuring the decay of photoluminescence over time. The decay profiles are fitted to a tri-exponential decay function (Equation S10) and is indicative of the lifetime of the photogenerated carriers (Table 3). The average lifetime of charge carriers is calculated, and a slower decay (longer lifetime) is generally correlated with a suppressed recombination rate, which is beneficial for photocatalytic activity [40,41]. The experimental TRPL decay curves for the doped photocatalysts fit well and the fitted decay times for  $\text{Cu-TiO}_2$ ,  $\text{Au-TiO}_2$ , and  $\text{Ag-TiO}_2$  are longer compared to undoped  $\text{TiO}_2$ , which corresponds well with the observed trends in the steady state PL spectra. This confirms that metal doping extends the charge carrier lifetime, with  $\text{Cu-TiO}_2$  showing the longest carrier lifetime of 1.2 ns from 0.21 ns for pristine  $\text{TiO}_2$ , thus implying the most effective charge separation among the studied samples.

Electrochemical impedance spectroscopy (EIS) analysis was carried under dark and light irradiation conditions to observe the ability of charge transfer and the resistance offered. The Nyquist plots were fitted to Randle circuit which distinctly illustrate the charge transfer resistance ( $R_{ct}$ ) at the electrode/electrolyte interface for the different catalyst samples corresponding to the radius of the fitted semicircle in Nyquist plot in Fig. 8A. Notably, under dark conditions, larger  $R_{ct}$  is observed,

**Table 3**

Triexponential decay parameters for pure  $\text{TiO}_2$  and metal-doped  $\text{TiO}_2$  (Cu, Ag, Au) catalysts: time constants ( $\tau$ ) and amplitudes (A).

M- $\text{TiO}_2$	$\tau_1$	A <sub>1</sub>	$\tau_2$	A <sub>2</sub>	$\tau_3$	A <sub>3</sub>
$\text{TiO}_2$	1.076284	32.09	2.152568	23.33	4.305137	44.58
$\text{Cu-TiO}_2$	1.4332	57.29	2.866399	8.52	5.732799	34.19
$\text{Ag-TiO}_2$	1.747299	51.68	3.494598	34.33	6.989196	13.99
$\text{Au-TiO}_2$	1.401625	35.40	2.803251	28.47	5.606502	36.13

which under illumination markedly reduces across all the photocatalysts, with metal doped ones exhibiting varied degrees of reduction in charge transfer resistances, indicative of their distinct roles in facilitating charge transfer processes [41,42]. This is particularly evident in the  $\text{Ag-TiO}_2$  samples, where the  $R_{ct}$  under light excitation is significantly lower than those in dark conditions, illustrating the efficacious role of silver in leveraging light to augment electron mobility followed by gold and copper respectively. Corroborating with the EIS findings, the linear sweep voltammetry (LSV) profiles further delineate the photocatalytic behaviour of these metal incorporated catalyst systems Fig. 8B. Under light conditions, the enhanced photocurrents affirm the generation of additional charge carriers, which actively participate in the redox processes. The onset potentials, shifts more positively for metal doped  $\text{TiO}_2$ , reflect the reduced energy barriers for the electrochemical reactions under illumination. Comparative analysis of the LSV curves reveals that Ag as a metal dopant is more effective in promoting photocurrent response with and without light, as evidenced by the higher current densities and the notable shift in onset potentials Fig. 8B. Additionally, one can observe the peak in the LSV profile at  $-0.2$  V, which can be attributed to the facilitated charge transfer from  $\text{TiO}_2$  to metal on light irradiation [43,44]. With, the larger metallic fraction of surface  $\text{Ag}^0$  species (Fig. 4) this peak is prominently observed in case of  $\text{Ag-TiO}_2$ .

The KPFM analysis potential mapping images reveals the variations in surface potential (Figure S8) for pure and M- $\text{TiO}_2$  samples ( $\text{Au-TiO}_2$ ,  $\text{Ag-TiO}_2$ , and  $\text{Cu-TiO}_2$ ). The surface potential is visualized through colour mapping. For pure  $\text{TiO}_2$ , it displays a relatively homogenous potential with low variation, indicating a consistent potential across the surface. Upon metal doping, there is a slight noticeable change in the surface potential, as seen by the contrast in the images Figure S8. The potential values for  $\text{Cu-TiO}_2$ ,  $\text{Au-TiO}_2$ , and  $\text{Ag-TiO}_2$  samples show significant variations, likely due to the introduction of metals, which have different electronic properties than  $\text{TiO}_2$ . The presence of metal particles can create localized areas with different work function values due to changes in the surface electronic structure. These changes are influenced

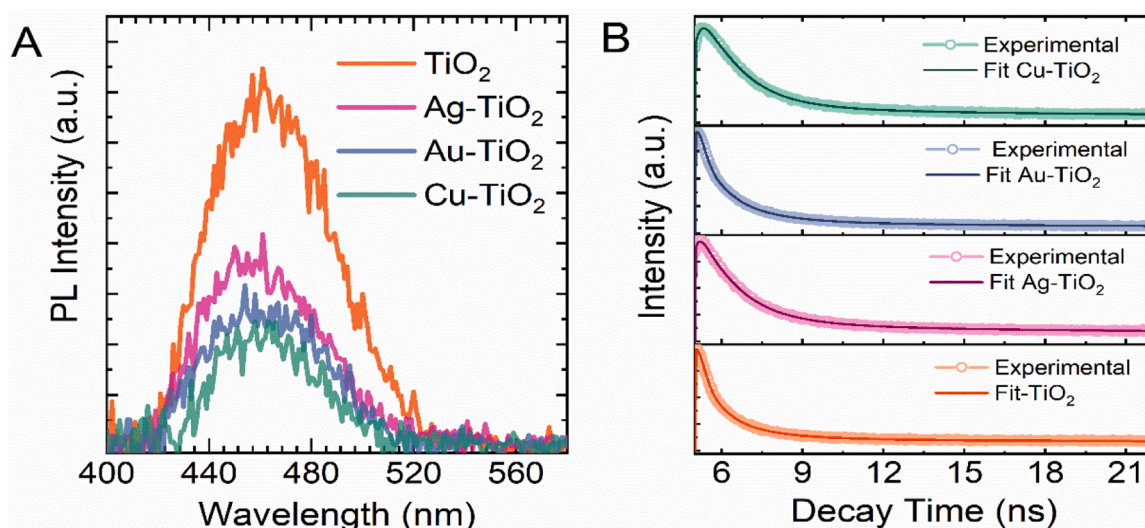


**Fig. 7.** Photoluminescence spectra (A) and time-resolved decay curves (B) of pure  $\text{TiO}_2$  and metal-doped  $\text{TiO}_2$  (Ag, Au, Cu) catalysts.



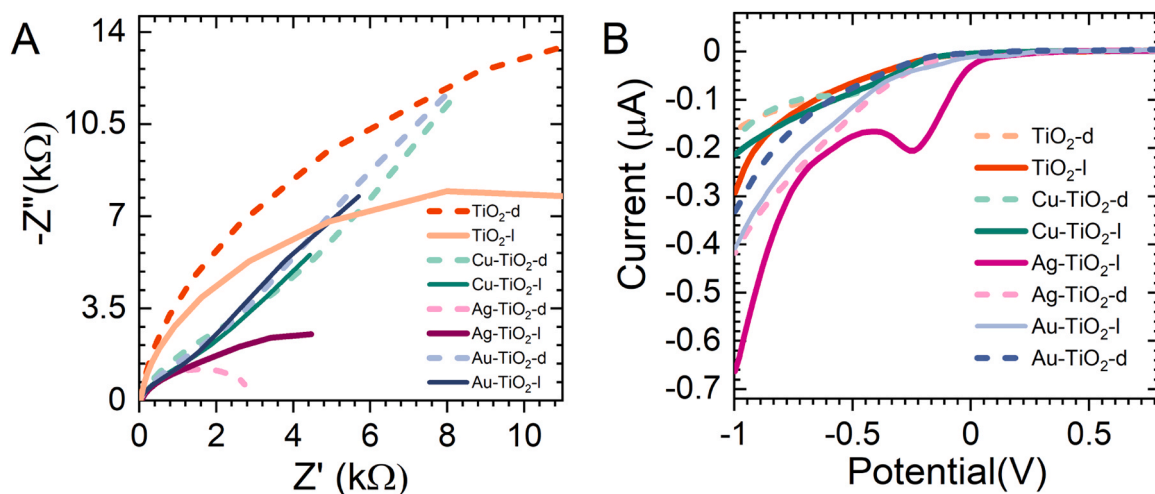


**Fig. 8.** Electrochemical impedance spectroscopy (EIS) Nyquist plots (A) and linear sweep voltammograms (B) for pure  $TiO_2$  and metal doped  $TiO_2$  (Ag, Au, Cu) under dark ('d') and light ('l') conditions.

by factors such as the type of metal, its oxidation state, particle size, and the interaction with the  $TiO_2$  support. For instance, noble metals like gold (Au) and silver (Ag) can introduce localized surface plasmon resonances, which may reduce the work function, while transition metals like copper (Cu) can donate electrons to the conduction band of  $TiO_2$ , affecting the surface potential. The observed differences can have important implications for catalytic activity, as areas with lower work function may facilitate electron transfer processes in photocatalytic reactions. The work function potential is also crucial in determining the energy alignment between the Fermi level of the metal and the conduction band of  $TiO_2$ , which is vital for efficient charge separation and transfer.

The Ultraviolet Photoelectron Spectroscopy (UPS) analysis of  $TiO_2$

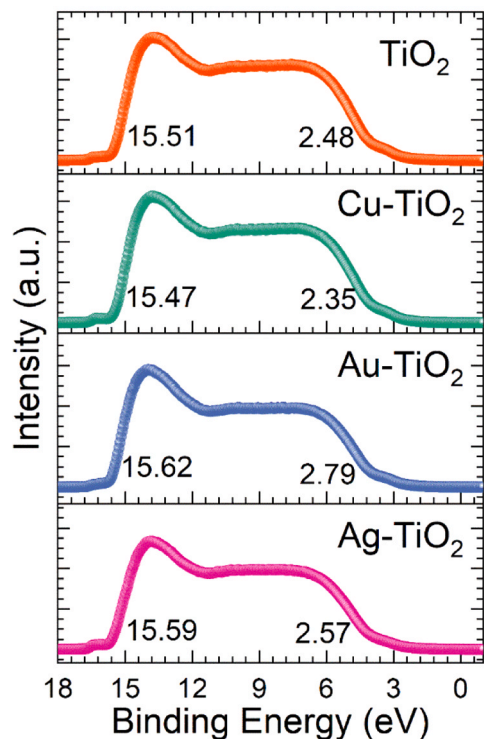


**Fig. 9.** Ultraviolet photoelectron spectroscopy (UPS) spectra showing valence band maxima for  $TiO_2$ , and metal doped  $TiO_2$  with copper (Cu), gold (Au), and silver (Ag).

and metal doped  $TiO_2$  samples as shown in Fig. 9. The work function ( $\Phi$ ) of each sample was deduced by subtracting the secondary electron cutoff ( $E_{cutoff}$ ) from the photon energy (21.22 eV) used in the UPS. Thus, evaluated work functions are 5.71 eV for  $TiO_2$ , 5.75 eV for  $Cu-TiO_2$ , 5.6 eV for  $Au-TiO_2$ , and 5.63 eV for  $Ag-TiO_2$ . These values indicate that  $Cu-TiO_2$  has a Fermi level ( $E_f$ ) closer to the valence band (VB), suggesting a potential for higher hole mobility compared to the other samples. From the UPS data it also provides insight into the valence band edge potentials, which are critical for understanding the electronic structure and potential photocatalytic performance of these materials. The valence band edge potential is seen to increase for the Cu-doped  $TiO_2$ , implying an upward shift in the potential scale, whereas for Au and Ag-doped materials, there is a decrease in comparison to pristine  $TiO_2$ .

This differential in Fermi level and valence band positioning reveals the unique electronic properties of Cu-doped  $TiO_2$ , which could lead to enhanced photocatalytic activities due to more favourable electron potentials. These shifts in electronic energy levels are vital for applications in photocatalysis and solar energy conversion, where the alignment of energy levels with respect to redox potentials determines the efficiency of charge transfer processes. The data suggests that Cu-doping could modulate the energy band structure of  $TiO_2$  in a way that potentially improves its interaction with light and its ability to drive photochemical reactions.

### 3.6. Performance toward $CO_2$ photocatalytic reduction activity

The comprehensive analysis of the photocatalytic reactivities of different metal-doped  $TiO_2$  catalysts (Fig. 10) in the gas-liquid-solid reaction medium reveals an interplay between metal type, loading, and the resulting product formation.

It is observed that, all  $TiO_2$ -based photocatalyst materials exhibit a preferential generation of hydrogen, primarily due to the better feasibility towards hydrogen generation or HER. However, it is noticeable that the ability to generate carbon-based products such as carbon monoxide (CO), methane ( $CH_4$ ) and methanol ( $CH_3OH$ ) varies significantly with the type and amount of metal doping. Copper (Cu) and silver (Ag) loaded  $TiO_2$  catalysts shows a marked inclination towards the formation of hydrogenated products. Among those, the Cu based  $TiO_2$  catalysts demonstrates a pronounced efficiency for  $CH_4/CH_3OH$  generation while Ag demonstrates pronounced CO generation ability. It is worth noting that there is no as such any optimized doping amount in this concentration domain, as the product formation rates doesn't show any significant decrement beyond any particular metal concentration.



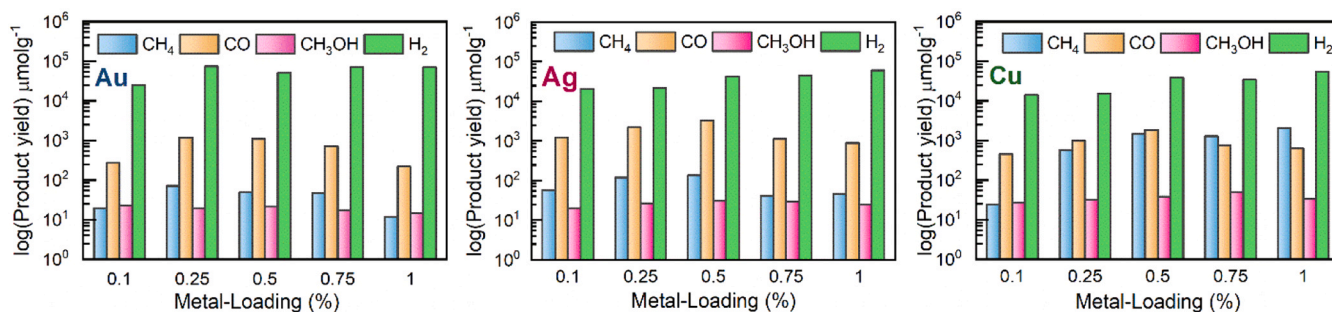


**Fig. 10.** Photocatalytic activity profiles for M-TiO<sub>2</sub> (M= Cu, Au, Ag) catalyst (5 mg in 5 ml solvent medium under 250 W Hg-Lamp) towards CH<sub>4</sub>, CO CH<sub>3</sub>OH and H<sub>2</sub> generation.

But for case of Cu, the photocatalytic CO<sub>2</sub> reduction activity is observed to be increasing with enhancement in the metal loading amounts. Additionally, Cu also shows the highest rates of CH<sub>3</sub>OH i.e., the liquid phase product formation as compared to Ag and Au metals. Based on the observed optical and electronic properties, the better carbonaceous product generation ability in case of Cu, can be expected due to the observed changes in the enhanced light absorption and lowered charge recombination as well as the positioning of bands, which is expected to enable the electronic transitions in such a way to minimize the charge carrier recombination in this light assisted transformation process. But in contrast, varied catalytic activity trends are observed, Au metal in particular showed highest yield towards hydrogen generation even with lower light absorption and higher recombination abilities. While for Cu, Ag the activity towards carbon-based products dominated in comparison to those observed in Au. This difference in carbon dioxide hydrogenated product yield and selectivity can be due to the distinct electronic properties imparted by the metal dopants. Au, as observed for its unique electronic configuration with plasmon bands as well as higher surface oxygen vacancy concentrations and catalytic properties like surface areas, exhibits the highest electron selectivity for the HER. Conversely, copper (Cu), with its d-orbitals conducive to CO<sub>2</sub> activation, shows enhanced selectivity towards CO<sub>2</sub> Reduction Reaction (CO<sub>2</sub>RR), aligning with the observed surge in carbonaceous products.

Defining the electron selectivity as to its involvement in the type of reduction process it is involved in among HER or CO<sub>2</sub>RR. In the radar chart representations (Fig. 11), which provide a visual summary of electron selectivity, the distinct catalytic behaviours of different metal

dopants are evident. The radar chart depicts metal loading amounts as radial axes (represented as 0.1, 0.25, 0.5, 0.75 and 1 on the vertices of pentagon) and electron selectivity ranges (represented along the axis from centre to vertex) for different reactions as pentagonal shapes, with distinct colors indicating specific metals. Au's apex in HER selectivity signifies its superior capacity for proton reduction, a trait potentially attributable to its better H<sub>2</sub>O reduction over the surface. In contrast, Cu's peak in CO<sub>2</sub>RR selectivity hints at a strong interaction between the metal and CO<sub>2</sub>, likely due to the optimal positioning of Cu's d-states that facilitates CO<sub>2</sub> adsorption and activation[43]. Understanding such variations are essential to not only understand the fundamental aspects of photocatalytic CO<sub>2</sub> reduction process but also for the rational design of tailored catalysts for specific target product from reaction. It is crucial to elucidate the other essential underlying factors which can govern selectivity and activity, so that one can fine-tune the catalyst systems for desired applications proceeding competently. Following section discusses the mechanistic aspects in M-TiO<sub>2</sub> system impacting such catalytic variations.

### 3.7. Insights into reactant adsorption mechanism

The efficiency of any catalytic processes is intimately dependent to the adsorptive interactions between the catalyst surface and substrate molecules. Our investigation into the affinity of CO<sub>2</sub> and H<sub>2</sub>O for metal loaded TiO<sub>2</sub> surfaces reveals substantial differences in substrate adsorption ability, which can have a significant implication for the catalytic performance. CO<sub>2</sub> temperature-programmed desorption (TPD)

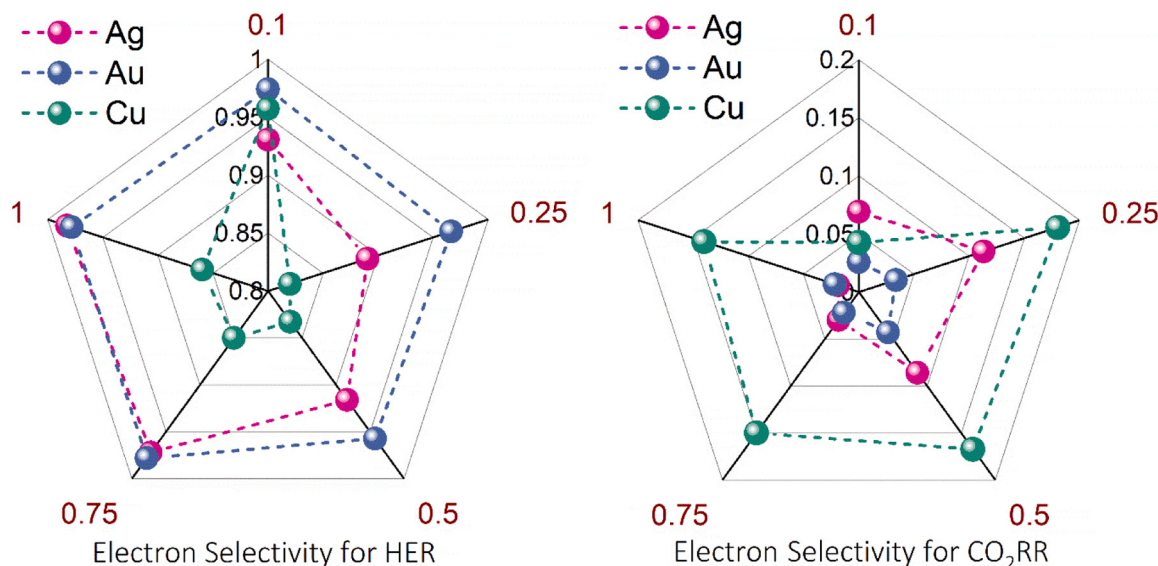


**Fig. 11.** Electron Selectivity comparison for HER or CO<sub>2</sub>RR for different metal loadings in M-TiO<sub>2</sub> (M= Cu, Au, Ag).

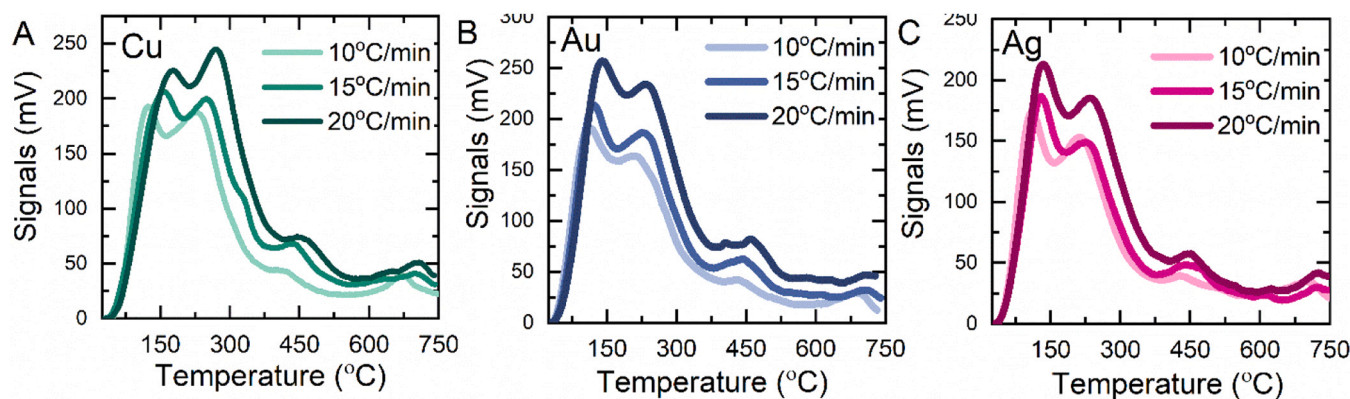


Fig. 12. CO<sub>2</sub> Temperature programmed desorption profiles at different ramp rates to evaluate the BE of different metals for M-TiO<sub>2</sub> (M= Cu, Au, Ag).

profiles (Fig. 12) indicate that for TiO<sub>2</sub> based samples, different kinds of basic sites are present corresponding to the observed peaks at certain desorption temperatures. Desorption peak at lower temperature corresponds to weak basic sites while those at subsequent temperatures corresponds to moderate and strong basic sites respectively[41]. For the copper loaded TiO<sub>2</sub> it exhibits a markedly higher CO<sub>2</sub> adsorption affinity compared to gold and silver as accounted by the total adsorbed CO<sub>2</sub> evaluated from area under the desorption profile. Additionally, the temperature profile for Cu, differs from Ag and Au demonstrating the different nature of available basic sites. The desorption peak located in the temperature range of 250–300°C, was more intense compared to that at 150°C, ascribing to the varying basicity of the metallic sites in different metals, showing predominance of weak basic sites for silver and gold, and relatively more presence of moderate basic sites for the copper-based materials. Further, the binding affinity for CO<sub>2</sub> is quantitatively assessed through the maxima of adsorption peaks across various heating rates demonstrated from Eq. 1.

$$2 \ln T_M - \ln \beta = \ln \left( \frac{E_a}{AR} \right) + \frac{E_a}{RT_M} \quad (1)$$

Where,  $T_M$  represents the temperature at which maxima is attained and  $E_a$  is the activation energy,  $A$ ,  $R$  are the Arrhenius and gas constants respectively and  $\beta$  is the ramp rate in the measurement (complete derivation in SI). Fig. 15 shows, with increasing temperature ramps the desorption peak shifts at higher temperature and the values of binding energy thus evaluated are depicted in Table 4, demonstrating that copper's multiple oxidation states confer a unique stabilization effect, thus promoting the CO<sub>2</sub> adsorption. The contact angle measurements serve as a proxy for H<sub>2</sub>O affinity, with copper and silver showing a lower contact angle, indicative of better wettability and, hence, superior H<sub>2</sub>O adsorption in comparison to gold (Table 4). The substrates (CO<sub>2</sub>, H<sub>2</sub>O) adsorption trends are aligned with the observed photocatalytic activity, where copper loaded TiO<sub>2</sub> catalysts demonstrating a higher propensity for hydrogenated products like CH<sub>4</sub> and CH<sub>3</sub>OH, corroborating with the enhanced CO<sub>2</sub>, H<sub>2</sub>O binding on its surface, thus promoting the CO<sub>2</sub> hydrogenation.

Table 4

Comparison of binding energies (BE) of CO<sub>2</sub> and contact angles for metal-doped TiO<sub>2</sub> catalysts: copper (Cu), gold (Au), and silver (Ag).

Metal	Contact Angle	Binding energy
Cu	21.3	0.97–13.3 kT
Au	42.7	0.7–3.8 kT
Ag	26.9	1–9.9 kT

### 3.8. In-situ study of photocatalytic CO<sub>2</sub> reduction reaction

#### 3.8.1. Substrate adsorption and activation before light irradiation

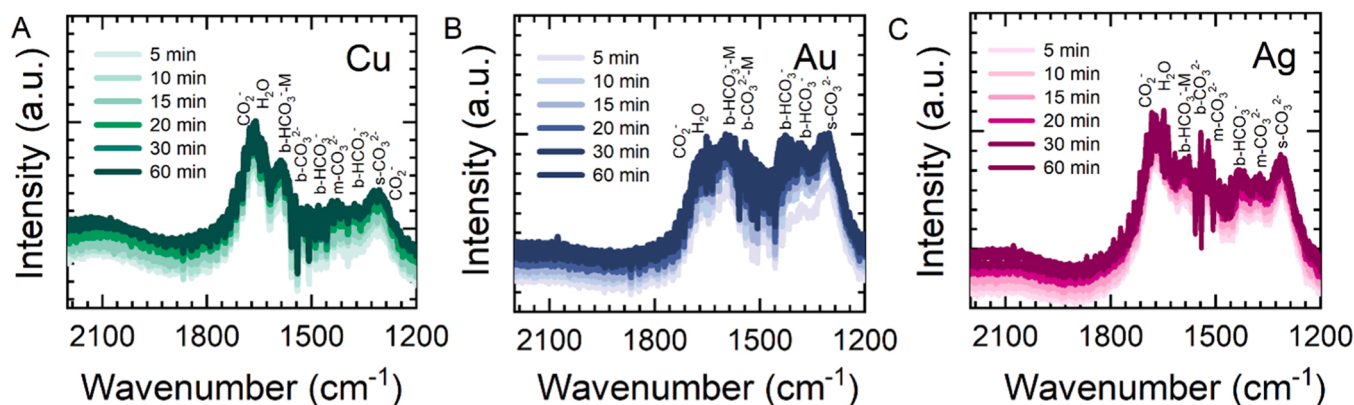
The Diffuse Reflectance Infrared Fourier Transform (DRIFT) spectroscopy results for M-TiO<sub>2</sub> catalysts exposed to a mixture of CO<sub>2</sub> and H<sub>2</sub>O vapours provide valuable insights into the adsorption mechanisms of these species over the catalyst surface (Fig. 13).

The data captured from 5 to 60-minute intervals after exposure to moist CO<sub>2</sub>, displays the evolution of adsorption intermediates over time. Upon exposure to CO<sub>2</sub> and H<sub>2</sub>O, the spectra reveal the immediate formation of distinct peaks at 1670 and 1247 cm<sup>-1</sup>, indicative of adsorbed H<sub>2</sub>O and CO<sub>2</sub> species in form of HCO<sub>3</sub><sup>-</sup> and CO<sub>3</sub><sup>2-</sup> onto the catalyst surface. These species are likely interacting with Ti<sup>3+</sup> ions, which may originate from oxygen vacancies present in the TiO<sub>2</sub> lattice[34]:



The rapid emergence of the several peaks (Fig. 13) suggests a dynamic equilibrium between the adsorption of various kinds of intermediates on the active sites of the catalyst. A persistent peak at approximately 1650 cm<sup>-1</sup> emerges in the spectra, attributed to the adsorption of H<sub>2</sub>O molecules. The spectra further identify the presence of various carbonate and bicarbonate species, including bidentate carbonates (b-CO<sub>3</sub><sup>2-</sup>) and bicarbonates (HCO<sub>3</sub><sup>-</sup>), alongside monodentate (m-CO<sub>3</sub><sup>2-</sup>, HCO<sub>3</sub><sup>-</sup>) and solvated (s-CO<sub>3</sub><sup>2-</sup>) counterparts[34,42]. The relative concentrations of these species differ based on the metal-substrate interaction, suggesting that the nature of the metal plays a crucial role in defining the adsorption landscape. In the case of Cu-TiO<sub>2</sub>, the DRIFT spectra highlight the predominance of surface-adsorbed carbonates and bicarbonates in mono- and bidentate configurations (Fig. 13A). For Au-TiO<sub>2</sub>, however, there is a notable concentration of solvated species, which resonate at lower wavenumbers, suggesting that the solvation environment around the gold sites has a significant influence on the adsorbed species (Fig. 13B)[45]. Ag-TiO<sub>2</sub> displays an intermediate behaviour with both surface-adsorbed and solvated species present in considerable amounts (Fig. 13C). These spectral features align with the proposed intermediates for CO<sub>2</sub> hydrogenation pathways, corroborating theoretical predictions[34,46]. Solvated carbonates can likely form via interactions between surface physisorbed carbonated species at the metal-TiO<sub>2</sub> interface[45]. While the surface bound species can interact with metal forming a chemical bond and interacting with present surface oxygen vacancies (O<sub>v</sub>) which can facilitate the stabilization of these intermediates. The electronic configuration, oxidation state, and interaction of the metal with the TiO<sub>2</sub> structure influence the concentration of oxygen vacancies at the metal-TiO<sub>2</sub> interfaces. For instance, the





different oxidation states of copper, as revealed by XPS, may explain the stabilization of surface-adsorbed species on Cu-TiO<sub>2</sub> interfaces. Moreover, the Cu-TiO<sub>2</sub> catalyst sample exhibit a strong adsorption of H<sub>2</sub>O, as evidenced by the infrared spectra. This could be attributed to the atomic configuration of copper, which may facilitate the dissociative adsorption of water, a phenomenon that has also been previously reported in the literature.

### 3.8.2. Substrate conversion mechanism after light irradiation

The followed observation of the infrared (IR) spectra under light irradiation reveals a significant insight into the photoreactive behaviour of M-TiO<sub>2</sub> catalysts (Fig. 14). Upon exposure to light irradiations, there's a noticeable decrease in the intensity of a few peaks adsorbed carbonate (CO<sub>3</sub><sup>2-</sup>), bicarbonate (HCO<sub>3</sub><sup>-</sup>), and surface adsorbed H<sub>2</sub>O species, indicating the desorption phenomenon from the catalyst surface due to their involvement in the photoreactions [33,34,47,48]. While an increase in

the peaks at 1370, 1492, and 1672  $\text{cm}^{-1}$  points to the rapid generation of hydrogenated intermediates under light. These peaks are tentatively assigned to various hydrogenated species like  $\text{HCHO}^*$ ,  $\text{CH}_2\text{O}^*$ ,  $\text{H}_3\text{C}^*$ , and  $\text{COOH}^*$ , like those evidenced from conversion experiments on  $\text{TiO}_2$  based catalyst systems[22,33,34,45,48–53]. Notably, peaks in 2071 and 1920  $\text{cm}^{-1}$  wavenumber emerges, which are likely due to CO surface species bonded in monodentate and bidentate configurations[53]. The spectra also reveal other intermediates such as  $\text{H}_3\text{CO}^*$  (1033  $\text{cm}^{-1}$ ),  $\text{CH}_3\text{O}^*$  (2954  $\text{cm}^{-1}$ ), and  $\text{CH}_2^*$  (2925  $\text{cm}^{-1}$ ) (Fig. 14 D, E, F), which play roles in the photocatalytic reduction product selectivity[41,51,52].

Additionally, oxygenated species bonded to the metal surfaces, indicated by peaks at 948 and 842  $\text{cm}^{-1}$ , correspond to metal-oxide (M=O) and metal-oxygen-metal (M-O-M) linkages (Fig. 14 A, B, C) [54]. Time-resolved spectral analysis across different metals illustrates the dynamic evolution of these intermediates. There's a higher concentration of hydrogenated species bound through oxygen on the

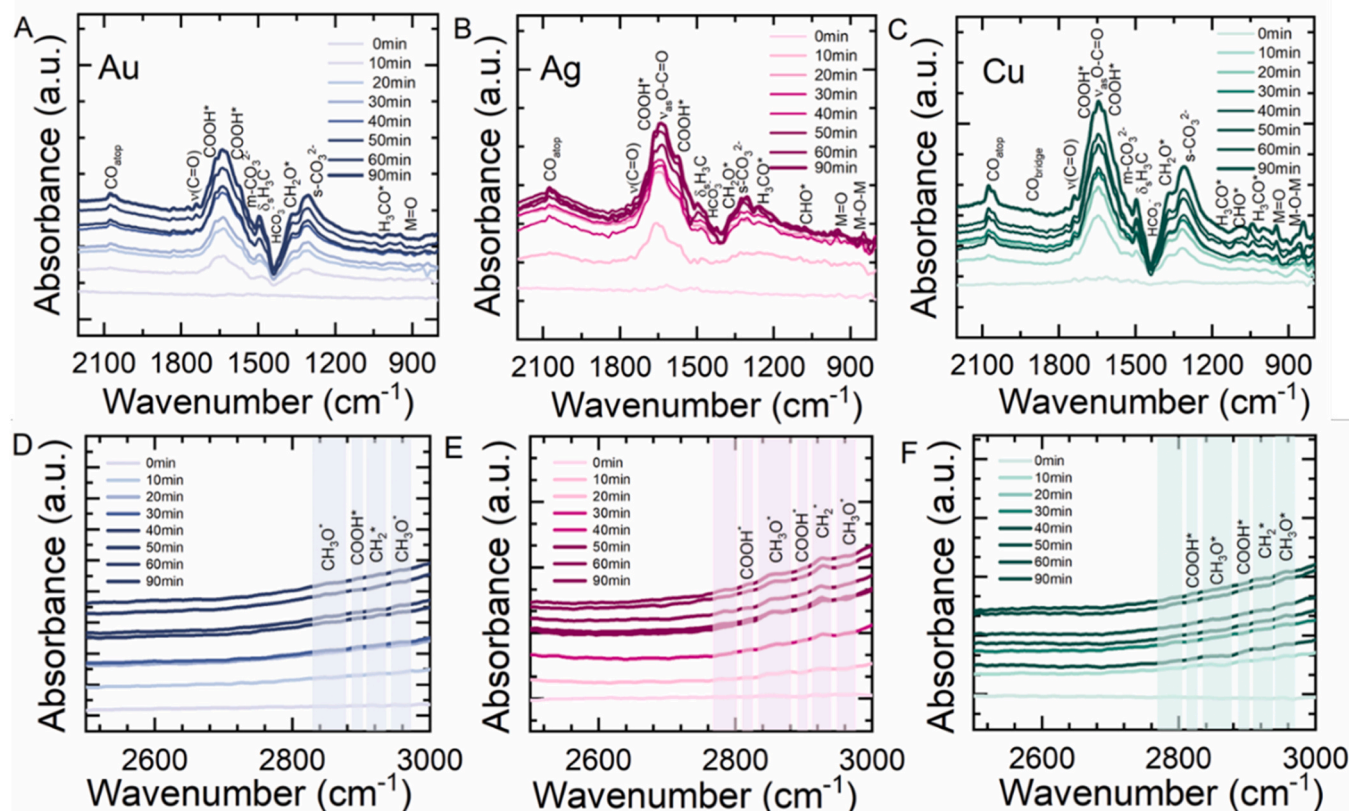


**Fig. 14.** The time-resolved DRIFT spectra of (A) Au (B) Ag and (C) Cu incorporated TiO<sub>2</sub> after light-on with corresponding peak assignments.



Cu-TiO<sub>2</sub>, suggesting effectiveness of Cu in stabilizing such intermediates. Product selectivity for carbon-based products is primarily influenced by the nature of the CO\* intermediate, with loosely bound monodentate CO leading to CO production and more tightly bound species undergoing further hydrogenation to form reduced products. Of hydrogenated products, formation of methane and methanol are the final C<sub>1</sub> based products[41]. Of which the methanol selectivity hinges on the stability of the H<sub>3</sub>CO\* intermediate, which can either dissociate to form CH<sub>4</sub> or undergo hydrogenation to yield CH<sub>3</sub>OH, depending on the strength of the oxygen-metal bond. This process is notably enhanced by the presence of M=O species, which are reactive and can convert CH<sub>4</sub> to CH<sub>3</sub>OH, a reaction particularly prevalent in Cu-doped TiO<sub>2</sub> [46]. For M-TiO<sub>2</sub>, the intermediates and their binding tendency with the surface affect the subsequent reaction pathway. In comparison to Au, both Cu and Ag favour surface-bound intermediates that undergo a sequence of hydrogenation steps consistent with either the formaldehyde or carbene pathways[55]. However, in the case of Cu-TiO<sub>2</sub>, the corresponding intermediate's stability suggests the predominance of the formaldehyde pathway, characterized by intermediates like CH<sub>3</sub>O\* and HCO\*. Meanwhile, Ag-TiO<sub>2</sub> tends to follow the carbene pathway, with CH<sub>2</sub>\* and CH<sub>3</sub>\* as the key intermediates observed.

### 3.9. CO chemisorption for insights into stabilization effects

To clearly underline the factor governing CO hydrogenation. Analysis of affinity on Ag, Cu-TiO<sub>2</sub> catalysts is investigated to understand the fine interplay of adsorption dynamics and surface chemistry, using CO Temperature-Programmed Desorption (CO-TPD) measurements. Fig. 15 indicates, for Ag-TiO<sub>2</sub>, TPD profiles indicate a preference for adsorbing CO in a weakly bound monodentate configuration. This weak binding can facilitate the desorption of CO at lower temperatures, which is presumed to be contributing to the selectivity of Ag-TiO<sub>2</sub> for CO as the primary product[52]. In contrast, Cu-TiO<sub>2</sub> exhibits moderate to strong binding sites for CO, as suggested by the higher desorption temperatures in the TPD spectrum. These stronger binding sites may hinder the desorption of CO, thereby favouring its hydrogenation to other products due to prolonged surface residence times. This characteristic significantly contributes to the enhanced production of hydrogenated compounds, such as methane and methanol, over Cu-TiO<sub>2</sub>.

## 4. Discussion

The structural integrity of the crystal, coupled with improved light absorption capabilities and extended charge carrier lifetimes, plays an important role in light-assisted transformations processes. Additionally, the optoelectronic properties of the system, particularly those associated with the electronic states of copper, are crucial. These states enable inter-band transitions, which facilitate the migration of electrons across

the catalyst's surface. This electron mobility is among the key factors in influencing the efficiency of the catalytic process, as it can directly impact the activation and conversion of reactants during photocatalysis. The presence of multiple oxidation states in the metal component further influences the reaction pathway followed for the reduction process. From the CO, CO<sub>2</sub>-TPD and IR spectroscopy, under light irradiation for the photoreactive surface chemistry of metal-doped TiO<sub>2</sub>, it demonstrates the crucial role of metal dopants in influencing the adsorption, desorption, and transformation of reactants, ultimately guiding the pathway and selectivity controlling parameters for the photocatalytic reduction processes. Based on the in-situ data and the observed photocatalytic activities, here we propose the following mechanistic pathways (Fig. 16) for the CO<sub>2</sub> photoreduction on TiO<sub>2</sub>-based catalysts. Both formaldehyde and the carbene pathways are operational in these systems. However, the predominant pathway appears to be dictated by the nature of the metal dopant, which influences the stabilization of various intermediate species. For Cu-TiO<sub>2</sub>, a significant following of the formaldehyde pathway is indicated by the strong presence of CH<sub>3</sub>O\* and M=O species in the DRIFTS spectra. These intermediates suggest that copper promotes the formation of formaldehyde (HCHO), methanol (CH<sub>3</sub>OH), and methane (CH<sub>4</sub>) through a series of hydrogenation steps, beginning with the initial activation of CO<sub>2</sub> to formate (HCOO\*) and further to methoxy (CH<sub>3</sub>O\*). In contrast, the predominance of CH<sub>2</sub>\* peaks in the spectra for Ag-TiO<sub>2</sub> points towards the carbene pathway being more influential. This pathway suggests that silver facilitates the formation of carbenes (CH<sub>2</sub>\*) as key intermediates, which can then either be hydrogenated to form methane (CH<sub>4</sub>) directly. For selective CH<sub>4</sub> and CH<sub>3</sub>OH formation, as observed in case of Cu, particularly noteworthy is the role of stabilized metal-oxygen (M=O) species for the transformation of methane to methanol over M=O sites in Cu-TiO<sub>2</sub>. The M=O species are implicated in the selective oxidation of methane, and the stability and reactivity of these (M=O) sites are crucial for promoting such oxidation reactions. Additionally, if the CO formation is desired, the active sites can be controlled to promote the weak adsorption of CO\* species over their surface. These mechanistic insights not only offer a detailed understanding of the catalytic CO<sub>2</sub> reduction processes but also highlight the critical role of metal dopants in determining the pathway selectivity. It presents the importance of rational tailoring the catalytic sites to modulate the product distribution in the photocatalysts.

## 5. Conclusion

The catalytic performance, in terms of both activity and product selectivity, is intricately linked to the combination of physical, optical, and electronic properties, along with the underlying reaction mechanism. The ability of the catalyst to absorb light and facilitate electronic transitions is significantly influenced by the nature of the metal dopant, its electronic configuration, and its interaction with TiO<sub>2</sub>. Furthermore, the lifetimes of charge carriers and the surface potentials are modulated by the positioning of the Fermi levels, which in turn affect the adsorption capabilities of the substrate as in case of copper doping, it enhances the adsorption of CO<sub>2</sub> and H<sub>2</sub>O on the catalyst surface, increasing the flux of reactants and potentially influencing their reduction phenomenon. Additionally, the stabilization of intermediates also is observed to be crucial for designing product selective catalysts. For selective generation of CO, the catalyst surface should be engineered to favour weak CO adsorption. Conversely, for enhanced methanol selectivity, the focus on augmenting the presence of reactive M=O species on the catalyst surface is observed to be essential. These insights are crucial for the strategic design of the catalysts, allowing for precise control over surface sites to promote certain reaction intermediates and pathways. Such tailored catalysts are key to achieving selectivity in the production of C<sub>1</sub> based products, depending on the intended application, thereby contributing to the advancement of photocatalytic CO<sub>2</sub> reduction technologies.

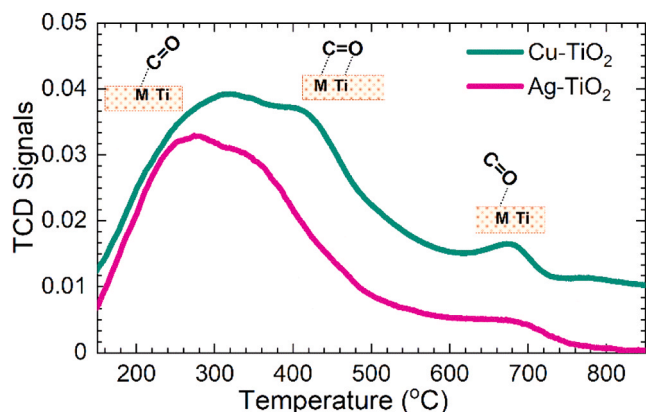
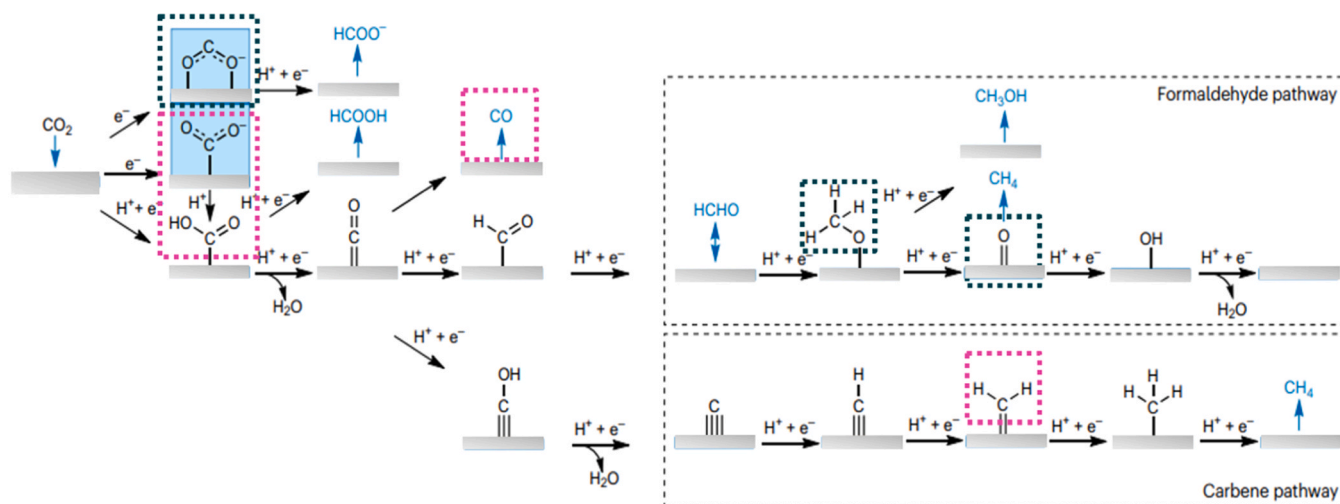


Fig. 15. CO temperature programmed desorption profile for Ag and Cu-TiO<sub>2</sub>.



**Fig. 16.** The scheme of plausible reaction pathway for CO, CH<sub>4</sub>, CH<sub>3</sub>OH production with boxed intermediates in green and pink demonstrating the stabilization over Cu and Ag surfaces.

### CRediT authorship contribution statement

**Shreya Singh:** Writing – review & editing, Writing – original draft, Visualization, Validation, Software, Methodology, Investigation, Formal analysis, Data curation, Conceptualization. **KAMAL K PANT:** Supervision, Project administration. **Raushan Kumar:** Resources, Data curation. **Sushant Kumar:** Writing – review & editing, Resources, Data curation. **Dhaval Kumar Joshi:** Visualization, Supervision, Resources, Data curation. **Pratim Biswas:** Supervision.

### Declaration of Competing Interest

The authors declare that they have no known competing financial interests or personal relationships that could have appeared to influence the work reported in this paper.

### Data availability

Data will be made available on request.

### Acknowledgements

SS acknowledges CRF and NRF facility at IIT Delhi.

### Appendix A. Supporting information

Supplementary data associated with this article can be found in the online version at [doi:10.1016/j.apcatb.2024.124054](https://doi.org/10.1016/j.apcatb.2024.124054).

### References

- [1] P.S. Basavarajappa, S.B. Patil, N. Ganganagappa, K.R. Reddy, A.V. Raghu, C. V. Reddy, Recent progress in metal-doped TiO<sub>2</sub>, non-metal doped/codoped TiO<sub>2</sub> and TiO<sub>2</sub> nanostructured hybrids for enhanced photocatalysis, *Int. J. Hydrog. Energy* 45 (2020) 7764–7778, <https://doi.org/10.1016/j.ijhydene.2019.07.241>.
- [2] A. Dhakshinamoorthy, S. Navalón, A. Corma, H. García, Photocatalytic CO<sub>2</sub> reduction by TiO<sub>2</sub> and related titanium containing solids, *Energy Environ. Sci.* 5 (2012) 9217–9233, <https://doi.org/10.1039/c2ee21948d>.
- [3] N. Shehzad, M. Tahir, K. Johari, T. Murugesan, M. Hussain, A critical review on TiO<sub>2</sub> based photocatalytic CO<sub>2</sub> reduction system: strategies to improve efficiency, *J. CO<sub>2</sub> Util.* 26 (2018) 98–122, <https://doi.org/10.1016/j.jcou.2018.04.026>.
- [4] S.N. Habisreutinger, L. Schmidt-Mende, J.K. Stolarczyk, Photocatalytic reduction of CO<sub>2</sub> on TiO<sub>2</sub> and other semiconductors, *Angew. Chem. Int. Ed.* 52 (2013) 7372–7408, <https://doi.org/10.1002/anie.201207199>.
- [5] X. Li, J. Yu, M. Jaroniec, X. Chen, Cocatalysts for selective photoreduction of CO<sub>2</sub> into solar fuels, *Chem. Rev.* 119 (2019) 3962–4179, <https://doi.org/10.1021/acs.chemrev.8b00400>.
- [6] S. Navalón, A. Dhakshinamoorthy, M. Álvaro, H. García, Photocatalytic CO<sub>2</sub> reduction using non-itanium metal oxides and sulfides, *ChemSusChem* 6 (2013) 562–577, <https://doi.org/10.1002/cssc.201200670>.
- [7] A.L. Linsebigler, G. Lu, J.T. Yates, Photocatalysis on TiO<sub>2</sub> surfaces: principles, mechanisms, and selected results, *Chem. Rev.* 95 (1995) 735–758, <https://doi.org/10.1021/cr00035a013>.
- [8] Z. Xiong, Z. Lei, Y. Li, L. Dong, Y. Zhao, J. Zhang, A review on modification of facet-engineered TiO<sub>2</sub> for photocatalytic CO<sub>2</sub> reduction, *J. Photochem. Photobiol. C. Photochem. Rev.* 36 (2018) 24–47, <https://doi.org/10.1016/j.jphotochemrev.2018.07.002>.
- [9] C.B. Almquist, P. Biswas, Role of synthesis method and particle size of nanostructured TiO<sub>2</sub> on its photoactivity, *J. Catal.* 212 (2002) 145–156, <https://doi.org/10.1006/jcat.2002.3783>.
- [10] Y.H. Hu, A highly efficient photocatalyst-hydrogenated black TiO<sub>2</sub> for the photocatalytic splitting of water, *Angew. Chem. - Int. Ed.* 51 (2012) 12410–12412, <https://doi.org/10.1002/anie.201206375>.
- [11] tefan Neatu, J.A. Maciá-Agulló, P. Concepción, H. García, Gold-copper nanoalloys supported on TiO<sub>2</sub> as photocatalysts for CO<sub>2</sub> reduction by water, *J. Am. Chem. Soc.* 136 (2014) 15969–15976, <https://doi.org/10.1021/ja506433k>.
- [12] O. Ola, M.M. Maroto-valer, Journal of photochemistry and photobiology c: photochemistry reviews review of material design and reactor engineering on TiO<sub>2</sub> photocatalysis for CO<sub>2</sub> reduction, *J. Photochem. Photobiol. C. Photochem. Rev.* 24 (2015) 16–42, <https://doi.org/10.1016/j.jphotochemrev.2015.06.001>.
- [13] K.A. Ali, A.Z. Abdullah, A.R. Mohamed, Visible light responsive TiO<sub>2</sub> nanoparticles modified using Ce and La for photocatalytic reduction of CO<sub>2</sub>: Effect of Ce dopant content, *Appl. Catal. A Gen.* 537 (2017) 111–120, <https://doi.org/10.1016/j.apcata.2017.03.022>.
- [14] L. Matějová, K. Kočí, M. Reli, L. Čapek, A. Hospodková, P. Peikertová, Z. Matěj, L. Obalová, A. Wach, P. Kuśrowski, A. Kotarba, Preparation, characterization and photocatalytic properties of cerium doped TiO<sub>2</sub>: on the effect of Ce loading on the photocatalytic reduction of carbon dioxide, *Appl. Catal. B Environ.* 152–153 (2014) 172–183, <https://doi.org/10.1016/j.apcatb.2014.01.015>.
- [15] X. Bi, G. Du, A. Kalam, D. Sun, Y. Yu, Q. Su, B. Xu, A.G. Al-Sehemi, Tuning oxygen vacancy content in TiO<sub>2</sub> nanoparticles to enhance the photocatalytic performance, *Chem. Eng. Sci.* 234 (2021) 116440, <https://doi.org/10.1016/j.ces.2021.116440>.
- [16] J. Xue, X. Jia, Z. Sun, H. Li, Q. Shen, X. Liu, H. Jia, Y. Zhu, Selective CO<sub>2</sub> photoreduction to C<sub>2</sub> hydrocarbon via synergy between metastable ordered oxygen vacancies and hydrogen spillover over TiO<sub>2</sub> nanobelts, *Appl. Catal. B Environ.* 342 (2024) 123372, <https://doi.org/10.1016/j.apcatb.2023.123372>.
- [17] K. Bhattacharyya, G.P. Mane, V. Rane, A.K. Tripathi, A.K. Tyagi, Selective CO<sub>2</sub> photoreduction with Cu-doped TiO<sub>2</sub> photocatalyst: delineating the crucial role of co-oxidation state and oxygen vacancies, *J. Phys. Chem. C.* (2021), <https://doi.org/10.1021/acs.jpcc.0c08441>.
- [18] E. Bahadori, A. Tripodi, A. Villa, C. Pirola, L. Prati, G. Ramis, N. Dimitratos, D. Wang, I. Rossetti, High pressure CO<sub>2</sub> photoreduction using Au/TiO<sub>2</sub>: unravelling the effect of co-catalysts and of titania polymorphs, *Catal. Sci. Technol.* 9 (2019) 2253–2265, <https://doi.org/10.1039/c9cy00286c>.
- [19] M. Tahir, B. Tahir, N.A.S. Amin, Synergistic effect in plasmonic Au/Ag alloy NPs co-coated TiO<sub>2</sub> NWs toward visible-light enhanced CO<sub>2</sub> photoreduction to fuels, *Appl. Catal. B Environ.* 204 (2017) 548–560, <https://doi.org/10.1016/j.apcatb.2016.11.062>.
- [20] J.Y. Do, R.K. Chava, K.K. Mandari, N.K. Park, H.J. Ryu, M.W. Seo, D. Lee, T. S. Senthil, M. Kang, Selective methane production from visible-light-driven photocatalytic carbon dioxide reduction using the surface plasmon resonance effect of superfine silver nanoparticles anchored on lithium titanium dioxide nanocubes (Ag@LiTiO<sub>2</sub>), *Appl. Catal. B Environ.* 237 (2018) 895–910, <https://doi.org/10.1016/j.apcatb.2018.06.070>.

- [21] M. Borges Ordoniño, A. Urakawa, Active surface species ruling product selectivity in photocatalytic CO<sub>2</sub> reduction over Pt- or Co-promoted TiO<sub>2</sub>, *J. Phys. Chem. C* 123 (2019) 4140–4147, <https://doi.org/10.1021/acs.jpcc.8b10814>.
- [22] Y. Yu, X. Dong, P. Chen, Q. Geng, H. Wang, J. Li, Y. Zhou, F. Dong, Synergistic effect of Cu single atoms and Au-Cu alloy nanoparticles on TiO<sub>2</sub> for efficient CO<sub>2</sub> photoreduction, *ACS Nano* 15 (2021) 14453–14464, <https://doi.org/10.1021/acsnano.1c03961>.
- [23] M. Sayed, L. Zhang, J. Yu, Plasmon-induced interfacial charge-transfer transition prompts enhanced CO<sub>2</sub> photoreduction over Cu/Cu<sub>2</sub>O octahedrons, *Chem. Eng. J.* 397 (2020) 125390, <https://doi.org/10.1016/j.cej.2020.125390>.
- [24] S. Singh, P. Tiwari, G. Venkanna, K.K. Pant, P. Biswas, The cooperative role of nitrogen defects and cyano-group functionalization in carbon nitride towards enhancing its CO<sub>2</sub> photoreduction activity, *Sustain. Energy Fuels* (2023), <https://doi.org/10.1039/D2SE01751B>.
- [25] N. Kumar Tailor, S. Singh, M.A. Afroz, K.K. Pant, S. Satapathi, Unraveling the impact of Cu-doping in lead free halide perovskites for markedly enhancing photocatalytic CO<sub>2</sub> reduction performance, *Appl. Catal. B Environ.* 340 (2024) 123247, <https://doi.org/10.1016/j.apcatb.2023.123247>.
- [26] Y. Zhao, I. Yavuz, M. Wang, M.H. Weber, M. Xu, J.H. Lee, S. Tan, T. Huang, D. Meng, R. Wang, J. Xue, S.J. Lee, S.H. Bae, A. Zhang, S.G. Choi, Y. Yin, J. Liu, T. H. Han, Y. Shi, H. Ma, W. Yang, Q. Xing, Y. Zhou, P. Shi, S. Wang, E. Zhang, J. Bian, X. Pan, N.G. Park, J.W. Lee, Y. Yang, Suppressing ion migration in metal halide perovskite via interstitial doping with a trace amount of multivalent cations, *2022 Nat. Mater.* 21 (2022) 1396–1402, <https://doi.org/10.1038/s41563-022-01390-3>.
- [27] P. Strasser, S. Koh, T. Anniyev, J. Greeley, K. More, C. Yu, Z. Liu, S. Kaya, D. Nordlund, H. Ogasawara, M.F. Toney, A. Nilsson, Lattice-strain control of the activity in dealloyed core-shell fuel cell catalysts, *2010 Nat. Chem.* 2 (2010) 454–460, <https://doi.org/10.1038/nchem.623>.
- [28] Y. Zhou, Q. Zhang, X. Shi, Q. Song, C. Zhou, D. Jiang, Photocatalytic reduction of CO<sub>2</sub> into CH<sub>4</sub> over Ru-doped TiO<sub>2</sub>: Synergy of Ru and oxygen vacancies, *J. Colloid Interface Sci.* 608 (2022) 2809–2819, <https://doi.org/10.1016/j.jcis.2021.11.011>.
- [29] B. Toubal, R. Bensaha, F. Yakuphanoglu, The influence of copper-cobalt co-doping on optical and electrical properties of nanostructures TiO<sub>2</sub> thin films prepared by sol-gel, *J. Sol. -Gel Sci. Technol.* 82 (2017) 478–489, <https://doi.org/10.1007/S10971-017-4337-8/TABLES/4>.
- [30] I. Ganesh, P.P. Kumar, I. Annappoorna, J.M. Sumliner, M. Ramakrishna, N. Y. Hebalkar, G. Padmanabham, G. Sundararajan, Preparation and characterization of Cu-doped TiO<sub>2</sub> materials for electrochemical, photoelectrochemical, and photocatalytic applications, *Appl. Surf. Sci.* 293 (2014) 229–247, <https://doi.org/10.1016/j.apsusc.2013.12.140>.
- [31] S. Singh, A. Modak, K.K. Pant, CO<sub>2</sub> reduction to methanol using a conjugated organic-inorganic hybrid TiO<sub>2</sub>-C<sub>3</sub>N<sub>4</sub> nano-assembly, *Trans. Indian Natl. Acad. Eng.* (2021) 1–10, <https://doi.org/10.1007/s41403-021-00201-6>.
- [32] J.H. Kim, G. Kwon, H. Lim, C. Zhu, H. You, Y.T. Kim, Effects of transition metal doping in Pt/M-TiO<sub>2</sub> (M = V, Cr, and Nb) on oxygen reduction reaction activity, *J. Power Sources* 320 (2016) 188–195, <https://doi.org/10.1016/j.jpowsour.2016.04.019>.
- [33] X. Zhang, X. Li, D. Zhang, N.Q. Su, W. Yang, H.O. Everitt, J. Liu, Product selectivity in plasmonic photocatalysis for carbon dioxide hydrogenation, *2017 Nat. Commun.* 8 (2017) 1–9, <https://doi.org/10.1038/ncomms14542>.
- [34] K. Wang, J. Lu, Y. Lu, C.H. Lau, Y. Zheng, X. Fan, Unravelling the CC coupling in CO<sub>2</sub> photocatalytic reduction with H<sub>2</sub>O on Au/TiO<sub>2</sub>-x: combination of plasmonic excitation and oxygen vacancy, *Appl. Catal. B Environ.* 292 (2021) 120147, <https://doi.org/10.1016/j.apcatb.2021.120147>.
- [35] R. Ravi, A.K. Golder, Bio-based Au doping with dominant oxygen vacancies and Ti<sup>3+</sup> defects on photocatalytic functionalities of TiO<sub>2</sub>, *Ind. Eng. Chem. Res.* 62 (2023) 20702–20715, [https://doi.org/10.1021/ACS.IECR.3C02850/SUPPL\\_FILE/IE3C02850\\_SI\\_001.PDF](https://doi.org/10.1021/ACS.IECR.3C02850/SUPPL_FILE/IE3C02850_SI_001.PDF).
- [36] C. Peng, P. Wei, X. Li, Y. Liu, Y. Cao, H. Wang, H. Yu, F. Peng, L. Zhang, B. Zhang, K. Lv, High efficiency photocatalytic hydrogen production over ternary Cu/TiO<sub>2</sub>@Ti<sub>3</sub>C<sub>2</sub>Tx enabled by low-work-function 2D titanium carbide, *Nano Energy* 53 (2018) 97–107, <https://doi.org/10.1016/j.nanoen.2018.08.040>.
- [37] J. Zhao, Y. Li, Y. Zhu, Y. Wang, C. Wang, Enhanced CO<sub>2</sub> photoreduction activity of black TiO<sub>2</sub>-coated Cu nanoparticles under visible light irradiation: role of metallic Cu, *Appl. Catal. A Gen.* 510 (2016) 34–41, <https://doi.org/10.1016/j.apcata.2015.11.001>.
- [38] G. Liu, L. Wang, H.G. Yang, H.M. Cheng, G.Q. Lu, Titania-based photocatalysts - Crystal growth, doping and heterostructuring, *J. Mater. Chem.* 20 (2010) 831–843, <https://doi.org/10.1039/b909930a>.
- [39] W. Hou, W.H. Hung, P. Pavaskar, A. Goepfert, M. Aykol, S.B. Cronin, Photocatalytic conversion of CO<sub>2</sub> to hydrocarbon fuels via plasmon-enhanced absorption and metallic interband transitions, *ACS Catal.* 1 (2011) 929–936, <https://doi.org/10.1021/cs2001434>.
- [40] S. Kumar, T. Malik, D. Sharma, A.K. Ganguli, NaNbO<sub>3</sub>/MoS<sub>2</sub> and NaNbO<sub>3</sub>/BiVO<sub>4</sub> core-shell nanostructures for photoelectrochemical hydrogen generation, *ACS Appl. Nano Mater.* 2 (2019) 2651–2662, <https://doi.org/10.1021/acsnanm.9b00098>.
- [41] J. Jiang, X. Wang, Q. Xu, Z. Mei, L. Duan, H. Guo, Understanding dual-vacancy heterojunction for boosting photocatalytic CO<sub>2</sub> reduction with highly selective conversion to CH<sub>4</sub>, *Appl. Catal. B Environ.* 316 (2022) 121679, <https://doi.org/10.1016/j.apcatb.2022.121679>.
- [42] S. Singh, R. Punia, K.K. Pant, P. Biswas, Effect of work-function and morphology of heterostructure components on CO<sub>2</sub> reduction photo-catalytic activity of MoS<sub>2</sub>-Cu<sub>2</sub>O heterostructure, *Chem. Eng. J.* 433 (2022) 132709, <https://doi.org/10.1016/j.cej.2021.132709>.
- [43] F. Xu, J. Mei, X. Li, Y. Sun, D. Wu, Z. Gao, Q. Zhang, K. Jiang, Heterogeneous three-dimensional TiO<sub>2</sub>/ZnO nanorod array for enhanced photoelectrochemical water splitting properties, *J. Nanopart. Res.* 19 (2017) 1–9, <https://doi.org/10.1007/S11051-017-3982-8/FIGURES/6>.
- [44] L. Guo, J. Cao, J. Zhang, Y. Hao, K. Bi, Photoelectrochemical CO<sub>2</sub> reduction by Cu<sub>2</sub>O/Cu<sub>2</sub>S hybrid catalyst immobilized in TiO<sub>2</sub> nanocavity arrays, *J. Mater. Sci.* 54 (2019) 10379–10388, <https://doi.org/10.1007/S10853-019-03615-4/FIGURES/5>.
- [45] L. Liu, X. Gu, Y. Cao, X. Yao, L. Zhang, C. Tang, F. Gao, L. Dong, Crystal-plane effects on the catalytic properties of Au/TiO<sub>2</sub>, *ACS Catal.* 3 (2013) 2768–2775, [https://doi.org/10.1021/CS400492W/SUPPL\\_FILE/CS400492W\\_SI\\_001.PDF](https://doi.org/10.1021/CS400492W/SUPPL_FILE/CS400492W_SI_001.PDF).
- [46] X. Zhang, X. Li, D. Zhang, N.Q. Su, W. Yang, H.O. Everitt, J. Liu, Product selectivity in plasmonic photocatalysis for carbon dioxide hydrogenation, *2017 Nat. Commun.* 8 (2017) 1–9, <https://doi.org/10.1038/ncomms14542>.
- [47] Y. Ku, L.M. Yan, G.K.T. Luong, Reduction of dissolved carbon dioxide in aqueous solution by UV-LED/TiO<sub>2</sub> process under periodic illumination, *J. CO<sub>2</sub> Util.* 41 (2020) 101283, <https://doi.org/10.1016/j.jcou.2020.101283>.
- [48] W. Shangguan, Q. Liu, Y. Wang, N. Sun, Y. Liu, R. Zhao, Y. Li, C. Wang, J. Zhao, Molecular-level insight into photocatalytic CO<sub>2</sub> reduction with H<sub>2</sub>O over Au nanoparticles by interband transitions, *2022 Nat. Commun.* 13 (2022) 1–11, <https://doi.org/10.1038/s41467-022-31474-2>.
- [49] N. Ojha, A. Bajpai, S. Kumar, Visible light-driven enhanced CO<sub>2</sub> reduction by water over Cu modified S-doped g-C<sub>3</sub>N<sub>4</sub>, *Catal. Sci. Technol.* 9 (2019) 4598–4613, <https://doi.org/10.1039/C9CY01185D>.
- [50] N. Ojha, S. Kumar, Tri-phase photocatalysis for CO<sub>2</sub> reduction and N<sub>2</sub> fixation with efficient electron transfer on a hydrophilic surface of transition-metal-doped MIL-88A (Fe), *Appl. Catal. B Environ.* 292 (2021) 120166, <https://doi.org/10.1016/j.apcatb.2021.120166>.
- [51] X. Wang, J. Jiang, Q. Xu, L. Duan, H. Guo, Understanding inclusive quantum dots hollow CN@CIZS heterojunction for enhanced photocatalytic CO<sub>2</sub> reduction, *Appl. Surf. Sci.* 604 (2022) 154601, <https://doi.org/10.1016/j.apsusc.2022.154601>.
- [52] J. Jiang, X. Wang, H. Guo, J. Jiang, X. Wang, H. Guo, Enhanced interfacial charge transfer/separation by LSPR-induced defective semiconductor toward high CO<sub>2</sub>RR performance, *Small* 19 (2023) 2301280, <https://doi.org/10.1002/SMLL.202301280>.
- [53] A. Wuttig, M. Yaguchi, K. Motobayashi, M. Osawa, Y. Surendranath, Inhibited proton transfer enhances Au-catalyzed CO<sub>2</sub>-to-fuels selectivity, *Proc. Natl. Acad. Sci. U. S. A.* 113 (2016) E4585–E4593, <https://doi.org/10.1073/PNAS.1602984113/-DCSUPPLEMENTAL/PNAS.201602984SI.PDF>.
- [54] J. Hu, L. Yu, J. Deng, Y. Wang, K. Cheng, C. Ma, Q. Zhang, W. Wen, S. Yu, Y. Pan, J. Yang, H. Ma, F. Qi, Y. Wang, Y. Zheng, M. Chen, R. Huang, S. Zhang, Z. Zhao, J. Mao, X. Meng, Q. Ji, G. Hou, X. Han, X. Bao, Y. Wang, D. Deng, Sulfur vacancy-rich MoS<sub>2</sub> as a catalyst for the hydrogenation of CO<sub>2</sub> to methanol, *2021 Nat. Catal.* 4 (2021) 242–250, <https://doi.org/10.1038/s41429-021-00584-3>.
- [55] S. Fang, M. Rahaman, J. Bharti, E. Reisner, M. Robert, G.A. Ozin, Y.H. Hu, Photocatalytic CO<sub>2</sub> reduction, *2023 Nat. Rev. Methods Prim.* 3 (2023) 1–21, <https://doi.org/10.1038/s43586-023-00243-w>.